

# Infrared 3–4 $\mu\text{m}$ Spectroscopic Investigations of a Large Sample of Nearby Ultraluminous Infrared Galaxies

Masatoshi Imanishi<sup>1,2</sup>

*National Astronomical Observatory, 2-21-1, Osawa, Mitaka, Tokyo 181-8588, Japan*

`masa.imanishi@nao.ac.jp`

C. C. Dudley

*Naval Research Laboratory, Remote Sensing Division, Code 7213, Building 2, Room 240B, 4555 Overlook Ave SW, Washington DC 20375-5351, U.S.A.*

`dudley@vivaldi.nrl.navy.mil`

and

Philip R. Maloney

*Center for Astrophysics and Space Astronomy, University of Colorado, Boulder, CO 80309-0389, U.S.A.*

`maloney@casa.colorado.edu`

## ABSTRACT

We present infrared  $L$ -band (3–4  $\mu\text{m}$ ) nuclear spectra of a large sample of nearby ultraluminous infrared galaxies (ULIRGs). ULIRGs classified optically as non-Seyferts (LINERs, HII-regions, and unclassified) are our main targets. Using the 3.3  $\mu\text{m}$  polycyclic aromatic hydrocarbon (PAH) emission and absorption features at 3.1  $\mu\text{m}$  due to ice-covered dust and at 3.4  $\mu\text{m}$  produced by bare

---

<sup>1</sup>Based in part on data collected at Subaru Telescope, which is operated by the National Astronomical Observatory of Japan.

<sup>2</sup>Visiting Astronomer at the Infrared Telescope Facility, which is operated by the University of Hawaii under Cooperative Agreement no. NCC 5-538 with the National Aeronautics and Space Administration, Office of Space Science, Planetary Astronomy Program.

carbonaceous dust, we search for signatures of powerful active galactic nuclei (AGNs) deeply buried along virtually all lines-of-sight. The  $3.3 \mu\text{m}$  PAH emission, the signatures of starbursts, is detected in all but two non-Seyfert ULIRGs, but the estimated starburst magnitudes can account for only a small fraction of the infrared luminosities. Three LINER ULIRGs show spectra typical of almost pure buried AGNs, namely, strong absorption features with very small equivalent-width PAH emission. Besides these three sources, 14 LINER and 3 HII ULIRGs' nuclei show strong absorption features whose absolute optical depths suggest an energy source more centrally concentrated than the surrounding dust, such as a buried AGN. In total, 17 out of 27 (63%) LINER and 3 out of 13 (23%) HII ULIRGs' nuclei show some degree of evidence for powerful buried AGNs, suggesting that powerful buried AGNs may be more common in LINER ULIRGs than in HII ULIRGs. The evidence of AGNs is found in non-Seyfert ULIRGs with both warm and cool far-infrared colors. These spectra are compared with those of 15 ULIRGs' nuclei with optical Seyfert signatures taken for comparison. The overall spectral properties suggest that the total amount of dust around buried AGNs in non-Seyfert ULIRGs is systematically larger than that around AGNs in Seyfert 2 ULIRGs. We argue that the optical (non-)detectability of Seyfert signatures in ULIRGs is highly dependent on how deeply buried the AGNs are, and that it is essential to properly evaluate the energetic importance of buried AGNs in non-Seyfert ULIRGs.

*Subject headings:* galaxies: active — galaxies: ISM — galaxies: nuclei — galaxies: Seyfert — galaxies: starburst — infrared: galaxies

## 1. Introduction

Ultraluminous infrared galaxies (ULIRGs), discovered by the *IRAS* all sky survey, radiate quasar-like luminosities ( $>10^{12}L_{\odot}$ ) as infrared dust emission (Sanders & Mirabel 1996). Powerful energy sources, starbursts and/or active galactic nuclei (AGNs), must be present hidden behind dust. This ULIRG population dominates not only the bright end of the local luminosity function (Soifer et al. 1987), but also the cosmic submillimeter background emission (Blain et al. 1999), so that their energy sources are closely related to understanding the connection between starbursts and AGNs.

It is now generally accepted that the majority of nearby ULIRGs are energetically dominated by compact ( $<500$  pc), highly dust-obscured nuclear cores, rather than extended ( $>kpc$ ), weakly-obscured starburst activity in host galaxies (Soifer et al. 2000; Fischer 2000).

Determining whether the compact cores are powered by AGNs and/or by very compact starbursts is essential, but it is not easy to distinguish the energy sources of ULIRGs' cores because the large amount of dust and molecular gas concentrated in the nuclei (Sanders & Mirabel 1996; Spoon et al. 2002) can hide the signatures of AGNs and make their detection difficult. If AGNs are obscured by dust in a *torus* geometry, as is inferred for some types of nearby AGN populations (Antonucci 1993), clouds along the torus axis are photo-ionized by the AGN's hard radiation. At  $\sim 100$  pc distances from the AGN, these clouds form the so-called narrow line regions (NLRs; Robson 1996), and the NLRs produce optical emission lines with flux ratios that are distinguishable from those of normal starburst galaxies (Veilleux & Osterbrock 1987). Thus, AGNs obscured by torus-shaped dust distributions can still be detectable through optical spectroscopy (classified as Seyfert 2 or Sy 2; Veilleux et al. 1999a). Such obscured AGNs with prominent NLRs are also recognizable through strong high-excitation forbidden line emission, originating in the NLRs, in high-resolution near- to mid-infrared spectra (Genzel et al. 1998; Veilleux et al. 1999b; Murphy et al. 2001; Armus et al. 2004). However, when virtually all directions around an AGN become opaque to the bulk of the AGN's ionizing photons (mostly soft X-rays and UV), no significant NLRs develop. In such *buried* AGNs, X-ray dissociation regions (XDRs), dominated by low-ionization species (Maloney et al. 1996) develop, rather than NLRs, so that the signatures of buried AGNs are difficult to find using the conventional searches for emission lines originating in the NLRs.

To study deeply buried AGNs without significant NLRs, observations at wavelengths of low dust extinction are necessary. Infrared *L*-band ( $\lambda = 2.8\text{--}4.1 \mu\text{m}$ ) spectroscopy from the ground is one of the most effective ways to find the signatures of such buried AGNs. First, dust extinction in the *L*-band is substantially reduced compared to shorter wavelengths ( $A_L \sim 0.06 \times A_V$ ; Rieke & Lebofsky 1985; Lutz et al. 1996) and is as low as that at 5–13  $\mu\text{m}$  (Lutz et al. 1996). Second, the contribution from AGN-powered dust emission to an observed flux, relative to stellar emission, increases substantially compared with  $\lambda < 2 \mu\text{m}$ . Thus, the detection of a buried AGN becomes more feasible than at  $\lambda < 2 \mu\text{m}$ . Third, normal starburst and AGN emission are clearly distinguishable using *L*-band spectra (Moorwood 1986; Imanishi & Dudley 2000). In a normal starburst galaxy, emission from polycyclic aromatic hydrocarbon (PAH) molecules is excited by far UV photons in photo-dissociation regions, the interfaces between molecular gas and HII-regions (Sellgren 1981; Normand et al. 1995). Near an AGN, the PAH molecules can be destroyed by strong X-ray radiation from the AGN (Voit 1992; Siebenmorgen et al. 2004). If the PAH molecules are sufficiently shielded by obscuration from the X-ray emission of the central AGN, the PAHs can survive. However, the far UV emission from the AGN will also be attenuated by the obscuration, so in a pure AGN without starburst activity, the PAH emission will be very weak. Instead, a featureless continuum from hot ( $\sim 1000$  K), submicron-sized dust grains

(Draine & Lee 1984; Mathis & Whiffen 1989) heated by the AGN is observed. If the AGN is deeply buried in dust, the  $3.1 \mu\text{m}$   $\text{H}_2\text{O}$  ice absorption feature produced by ice-covered dust and/or the  $3.4 \mu\text{m}$  absorption feature resulting from bare carbonaceous dust should be observed (Imanishi & Dudley 2000; Imanishi et al. 2001; Imanishi & Maloney 2003). In reality in ULIRGs, starbursts and AGNs are likely to coexist. Hence it is important to disentangle the energy sources of such starburst/AGN composite ULIRGs. This can be done using observations of PAH emission: because the column densities and pressures in the interstellar medium of ULIRGs are very high, the starburst regions in starburst/AGN composite ULIRGs should produce strong PAH emission (Maloney 1999). In a pure normal starburst galaxy, the equivalent width ( $\equiv$  a line-to-continuum flux ratio) of the  $3.3 \mu\text{m}$  PAH emission feature should always be high, regardless of dust extinction of the starburst (Moorwood 1986; Imanishi & Dudley 2000), because both the PAH and continuum emission are similarly flux-attenuated. If PAH emission is detected in a ULIRG, but its equivalent width is substantially smaller than in normal starburst galaxies, it will strongly suggest that the PAH equivalent width is being reduced by the contribution to the observed spectrum of a PAH-free featureless continuum, produced by the AGN. Thus, the presence of a powerful AGN can be inferred from the equivalent width of the  $3.3 \mu\text{m}$  PAH emission feature and dust absorption features, even if the AGN is buried.

In addition, using  $L$ -band spectra we have another independent way to detect the presence of powerful buried AGNs in ULIRGs: the absolute optical depth of dust absorption features. In a normal starburst, the energy sources (stars) and dust are spatially well mixed, while in a buried AGN, the energy source is very compact and thus should be more centrally concentrated than the surrounding dust (Soifer et al. 2000; Imanishi & Maloney 2003; Siebenmorgen et al. 2004). In the mixed dust/source geometry, the foreground less-obscured emission (which thus shows only weak absorption features) dominates the observed fluxes, and therefore there are upper limits to the absorption optical depths, unless unusual abundances are considered and/or there is a very large amount of foreground dust in the host galaxy (Imanishi & Maloney 2003). On the other hand, a centrally-concentrated energy source can show arbitrarily large optical depth, because a foreground screen dust extinction model is applicable (Imanishi & Maloney 2003). A few ULIRGs have been found to show substantially larger optical depths than the upper limits estimated for mixed dust/source geometry, and thus suggest centrally-concentrated energy sources (e.g., UGC 5101 and IRAS 08572+3915; Imanishi & Dudley 2000; Imanishi et al. 2001; Imanishi & Maloney 2003). These sources also display signatures of buried AGNs based on the equivalent width of the  $3.3 \mu\text{m}$  PAH emission (Imanishi & Dudley 2000; Imanishi et al. 2001) and observations at other wavelengths (Dudley & Wynn-Williams 1997; Soifer et al. 2000; Imanishi et al. 2003), demonstrating that this second method can also be applied to investigate the energy sources

of ULIRGs.

A number of papers have presented  $L$ -band spectra of nearby ULIRGs (Imanishi & Dudley 2000; Imanishi et al. 2001; Imanishi & Maloney 2003; Risaliti et al. 2003, 2005) and their energy sources have been investigated. However, the number of the observed sources is still too small to draw statistically meaningful conclusions. In this paper, we present ground-based  $L$ -band spectra of a large sample of nearby ULIRGs. Throughout this paper,  $H_0 = 75 \text{ km s}^{-1} \text{ Mpc}^{-1}$ ,  $\Omega_M = 0.3$ , and  $\Omega_\Lambda = 0.7$  are adopted. The physical scale of  $1''$  is 0.34 kpc in the nearest source at  $z = 0.018$ , 0.91 kpc at  $z = 0.05$ , and 2.44 kpc in the furthest source at  $z = 0.15$ .

## 2. Target

ULIRGs in the *IRAS* 1 Jy sample (Kim & Sanders 1998), with no obvious Seyfert signatures in the optical (non-Seyfert ULIRGs), are our main targets to look for buried AGNs. We restrict the sample to those at  $z \leq 0.15$  so that the long wavelength side of the redshifted  $3.4 \mu\text{m}$  dust absorption feature is at  $\lambda < 4.1 \mu\text{m}$ ; beyond this wavelength the steeply increasing Earth’s atmospheric background signal degrades spectral quality drastically in the case of ground-based observations. A declination cutoff  $> -26^\circ$  was also applied so that the targets are observable with small airmasses from Mauna Kea, Hawaii, our main observing site. These selection criteria result in 24 ULIRGs classified optically as LINERs, 17 ULIRGs classified optically as HII regions, and 4 optically unclassified ULIRGs, at  $z < 0.15$  in this sample, where the optical classifications are based on Veilleux et al. (1999a; their Table 2).

We gave highest priority to LINER ULIRGs because a pure buried AGN is expected to produce X-ray dissociation regions (Maloney et al. 1996) and to show a LINER-type optical spectrum (Imanishi et al. 2001). All 24 LINER ULIRGs were observed, comprising a complete sample. For the HII and unclassified ULIRGs, 11 (out of 17) and 2 (out of 4) sources were observed, respectively. One ULIRG, IRAS 13443+0822, consists of north-eastern and south-western nuclei, which are optically classified as an HII region and a Sy 2, respectively (Veilleux et al. 1999a). Although this ULIRG is classified as Sy 2 for the whole system (Veilleux et al. 1999a, their Table 2), we observed only the north-eastern HII nucleus. We include this source in the category of HII ULIRGs, raising the number of observed HII ULIRGs to 12. The observed 12 HII ULIRGs also constitute a complete sample, in the right ascension range 10–21 hr. The details of the observed non-Seyfert ULIRGs are summarized in Table 1.

In addition to these non-Seyfert ULIRGs, several ULIRGs with obvious Seyfert signa-

tures in the optical were also observed as a control sample. There are 12 Sy 2 ULIRGs at  $z < 0.15$  and declination  $> -26^\circ$  in the *IRAS* 1 Jy sample, excluding the above-mentioned IRAS 13443+0822. In total, 7 Sy 2 ULIRGs (Table 1) were observed. The main aims of observing these Sy 2 ULIRGs are twofold: (1) to check if our *L*-band spectroscopic method can successfully find signatures of obscured AGNs in these ULIRGs which we know possess obscured AGNs, and (2) to provide a control sample with which the properties of buried AGNs in non-Seyfert ULIRGs can be compared.

*L*-band spectra of several Sy 1 ULIRGs were also obtained. For these unobscured AGNs, since no significant  $3.4 \mu\text{m}$  dust absorption feature is expected, we extend the redshift restriction to  $z < 0.17$  where the longer wavelength side of the  $3.3 \mu\text{m}$  PAH emission feature is covered in the ground-based *L*-band spectrum. There are 7 Sy 1 ULIRGs at  $z < 0.17$  with declination  $> -26^\circ$  in the *IRAS* 1 Jy sample, and all of these sources were observed (Table 1).

### 3. Observations and Data Analysis

Observations were made primarily using the IRCS near-infrared spectrograph (Kobayashi et al. 2000) on the Subaru 8.2m telescope (Iye et al. 2004). Several bright ULIRGs were observed with CGS4 (Mountain et al. 1990) on the UKIRT 3.6m telescope, and with SpeX (Rayner et al. 2003) and NSFCAM (Shure et al. 1994) on the IRTF 3m telescope. Table 2 provides a detailed observing log.

For the Subaru IRCS observing runs, the sky was clear during the observations of all but one ULIRG (IRAS 16090–0139). The seeing at *K*, measured in images taken before *L*-band spectroscopy, was  $0''.4$ – $0''.9$  full-width at half maximum (FWHM). A  $0''.9$ -wide slit and the *L*-grism were used with a 58-mas pixel scale. The achievable spectral resolution is  $R \sim 140$  at  $\lambda \sim 3.5 \mu\text{m}$ . A standard telescope nodding technique (ABBA pattern), with a throw of  $7$ – $10''$  along the slit, was employed to subtract background emission. The optical guider of the Subaru telescope was used to monitor the telescope tracking. Exposure time was  $1.5$ – $2.5$  sec, and  $15$ – $40$  coadds were made at each nod position.

The spectra of two bright ULIRGs, IRAS 08572+3915 and Mrk 1014, were taken using IRTF SpeX (Rayner et al. 2003). The  $1.9$ – $4.2 \mu\text{m}$  cross-dispersed mode with a  $1''.6$  wide slit was employed. This mode enables *L*- ( $2.8$ – $4.1 \mu\text{m}$ ) and *K*-band ( $2$ – $2.5 \mu\text{m}$ ) spectra to be obtained simultaneously, with a spectral resolution of  $R \sim 500$ . The sky conditions were photometric throughout the observations, and the seeing at *K* was measured to be in the range  $0''.5$ – $0''.8$  FWHM. A standard telescope nodding technique (ABBA pattern) with

a throw of  $7''.5$  was employed along the slit. The telescope tracking was monitored with the infrared slit-viewer of SpeX. Each exposure was 15 sec, and 2 coadds were made at each position.

For the IRTF NSFCAM observations of IRAS 07599+6508, 3C 273, and IRAS 15462–0450, we used the NSFCAM grism mode (Shure et al. 1994). Sky conditions were photometric throughout the observations, and the seeing FWHM was measured to be  $0''.5$ – $0''.9$  in the  $K$ -band. The HKL grism and L blocker were used with the 4-pixel slit ( $= 1''.2$ ). The resulting spectral resolution was  $R \sim 150$  at  $\lambda \sim 3.5 \mu\text{m}$ . A standard  $10''$  telescope nodding technique (ABBA pattern) was employed. Each exposure was 1 sec, and 30 coadds were made at each nod position. An optical guide star was used for the telescope tracking, and the objects were observed in the eastern sky, where the tracking performance was well confirmed.

Spectra of four ULIRGs (Arp 220, IRAS 05189–2524, Mrk 273, Mrk 231) were taken with UKIRT CGS4 (Mountain et al. 1990), using a  $1''.2$  wide slit, and were published in Imanishi & Dudley (2000). The observing details are found in that paper.

For all the observing runs, A-, F-, and G-type main sequence stars (Table 2) were observed as standard stars, with mean airmass difference of  $<0.1$  to the individual ULIRGs' nuclei, to correct for the transmission of the Earth's atmosphere and to provide flux calibration. The  $L$ -band magnitudes of the standard stars were estimated from their  $V$ -band ( $\lambda = 0.6 \mu\text{m}$ ) magnitudes, adopting the  $V - L$  colors appropriate to the stellar types of individual standard stars (Tokunaga 2000).

Standard data analysis procedures were employed, using IRAF<sup>1</sup>. Initially, frames taken with an A (or B) beam were subtracted from frames subsequently taken with a B (or A) beam, and the resulting subtracted frames were added and divided by a spectroscopic flat image. Then, bad pixels and pixels hit by cosmic rays were replaced with the interpolated values of the surrounding pixels. Finally the spectra of ULIRGs' nuclei and standard stars were extracted, by integrating signals over  $0''.9$ – $2''.0$ , depending on actual signal profiles. Wavelength calibration was performed taking into account the wavelength-dependent transmission of the Earth's atmosphere. The spectra of ULIRGs' nuclei were divided by the observed spectra of standard stars, multiplied by the spectra of blackbodies with temperatures appropriate to individual standard stars (Table 2).

Flux calibration for all ULIRGs but one (IRAS 16090–0139) was done based on signals

---

<sup>1</sup>IRAF is distributed by the National Optical Astronomy Observatories, which are operated by the Association of Universities for Research in Astronomy, Inc. (AURA), under cooperative agreement with the National Science Foundation.

of ULIRGs and standard stars detected inside our slit spectra. For the Subaru IRCS spectrum of IRAS 16090–0139, since its spectrum was taken under non-photometric conditions, we calibrated its flux level based on our own  $L$ -band photometry ( $L = 13.3$ ), made on a different night using IRTF NSFCAM. Seeing sizes at  $K$  (and  $L$ ) were always smaller than the employed slit widths, and good telescope tracking performances of Subaru, IRTF, and UKIRT were established. We thus expect possible slit loss to be minimal. To estimate this ambiguity, we divided the whole data set into sub-groups and compared their flux levels. With the exception of the highly time variable source 3C 273, the flux levels agree within 10% for most objects and 30% for the worst case, suggesting that the flux uncertainty is at a similar level, which will not affect our main conclusions significantly. For 3C 273, time variation was clearly recognizable even during our IRTF NSFCAM observing run. For this source, the resulting spectrum is a time averaged one.

To obtain an adequate signal-to-noise ratio in each element, appropriate binning of spectral elements was performed, particularly at  $\lambda_{\text{obs}} < 3.3 \mu\text{m}$  in the observed frame, where the scatter of data points is larger, due to poorer Earth atmospheric transmission, than at  $\lambda_{\text{obs}} > 3.4 \mu\text{m}$ . The resulting spectral resolution at  $\lambda_{\text{obs}} < 3.3 \mu\text{m}$  is  $R \lesssim 100$  in most cases. The atmospheric transmission curve at  $\lambda_{\text{obs}} = 2.8\text{--}3.3 \mu\text{m}$  is fairly smooth at this spectral resolution. Thus, even if the net positions of the target object and standard star on the slit differ slightly (on the sub-pixel scale) along the wavelength direction, the standard data analysis described above is expected to produce no significant spurious features in spectra with  $R \lesssim 100$  (see Imanishi & Maloney 2003).

## 4. Results

### 4.1. $L$ -band spectra

Figures 1, 2, 3, 4, and 5 present flux-calibrated  $L$ -band spectra of the nuclei of ULIRGs optically classified as LINERs, HII-regions, unclassified, Sy 2, and Sy 1, respectively. For ULIRGs which have more than one nuclei brighter than  $L \sim 14.5$  mag, spectra of individual nuclei are shown separately. The total number of  $L$ -band spectra is 27 for LINER, 13 for HII, 2 for unclassified, 8 for Sy 2, and 7 for Sy 1 ULIRGs' *nuclei*.  $L$ -band spectra of several ULIRGs' nuclei, previously presented by Imanishi & Dudley (2000) and Imanishi & Maloney (2003), are shown again here.

There are a variety of spectral shapes, but the majority of the observed ULIRGs show emission features at  $\lambda_{\text{obs}} = (1 + z) \times 3.29 \mu\text{m}$ , the wavelength where the  $3.3 \mu\text{m}$  PAH emission feature has a peak. We thus identify these features as the  $3.3 \mu\text{m}$  PAH emission.



To estimate the strength of the 3.3  $\mu\text{m}$  PAH emission feature in the spectra where broad absorption features coexist and overlap with the PAH emission feature in wavelength, we make the reasonable assumption that the profiles of the 3.3  $\mu\text{m}$  PAH emission in these ULIRGs are similar to those of Galactic star-forming regions and nearby starburst galaxies; the main emission profile extends between  $\lambda_{\text{rest}} = 3.24\text{--}3.35 \mu\text{m}$  in the rest frame (Tokunaga et al. 1991; Imanishi & Dudley 2000). Data points at slightly shorter than  $\lambda_{\text{rest}} = 3.24 \mu\text{m}$  and slightly longer than  $\lambda_{\text{rest}} = 3.35 \mu\text{m}$ , unaffected by obvious absorption features, are adopted as the continuum levels to estimate the 3.3  $\mu\text{m}$  PAH emission strength. We adopt the spectral profile of type-1 sources (Tokunaga et al. 1991) as a template for the 3.3  $\mu\text{m}$  PAH emission. The adopted template reproduces the observed 3.3  $\mu\text{m}$  PAH emission features of the ULIRGs reasonably well, with our spectral resolution and signal-to-noise ratios. Table 3 summarizes the fluxes, luminosities, and rest-frame equivalent widths ( $\text{EW}_{3.3\text{PAH}}$ ) of the 3.3  $\mu\text{m}$  PAH emission feature. The uncertainties of the 3.3  $\mu\text{m}$  PAH emission fluxes, estimated from the fittings, are  $<20\%$  in most cases, and  $\sim 30\%$  even for ULIRGs with large scatters at the wavelengths around the 3.3  $\mu\text{m}$  PAH emission. We also tried several continuum levels in a reasonable range, to estimate possible systematic uncertainties coming from continuum determination ambiguities. The estimated 3.3  $\mu\text{m}$  PAH emission fluxes usually agree within 20% for ULIRGs with smooth continuum emission. Even in ULIRGs with winding spectra, the estimated fluxes do not differ by  $>30\%$ , as long as reasonable continuum levels are adopted. Thus, the total PAH flux uncertainties are unlikely to exceed  $\sim 40\%$  even in the worst case.

In addition to the 3.3  $\mu\text{m}$  PAH emission feature, clear absorption features at  $\lambda_{\text{rest}} = 3.4 \mu\text{m}$  by bare carbonaceous dust (Pendleton et al. 1994) was found in three LINER ULIRGs, IRAS 08572+3915NW, 12127–1412NE, and 17044+6720 (Figure 1), and one Sy 2 ULIRG, IRAS 12072–0444N (Figure 4). The unobscured  $L$ -band spectral shapes of AGNs are dominated by hot dust emission and almost linear (Imanishi 2002, 2003; Imanishi & Wada 2004). Starburst galaxies also show  $L$ -band spectra that are approximately linear, aside from the 3.3  $\mu\text{m}$  PAH emission feature (Imanishi & Dudley 2000). To estimate the optical depths of the 3.4  $\mu\text{m}$  carbonaceous dust absorption features, we therefore adopt a linear continuum, which is shown as a dashed line in the spectra of these four ULIRGs in Figures 1 and 4. The estimated optical depths of the 3.4  $\mu\text{m}$  absorption feature ( $\tau_{3.4}$ ) for these ULIRGs are summarized in Table 4.

In the observed spectra of many ULIRGs, other important features are present: (1) There is a spectral “gap”, in that the flux densities at the shorter wavelength side of the 3.3  $\mu\text{m}$  PAH emission feature are fainter than the extrapolation from the data points at the longer wavelength side. (2) The continuum is concave. At the shorter wavelength side of the 3.3  $\mu\text{m}$  PAH emission, the continuum flux level initially decreases with decreasing wavelength,

but then begins to increase again at  $\lambda_{\text{rest}} \sim 3.05 \mu\text{m}$ , and then the spectra become flat at the shortest wavelengths ( $\lambda_{\text{rest}} < 2.7 \mu\text{m}$ ). This behavior is naturally explained by the broad H<sub>2</sub>O ice absorption feature caused by ice-covered dust grains (Spoon et al. 2000; Imanishi & Maloney 2003). The signatures of this feature are found in none of the Sy 1 ULIRGs, as expected from the unobscured view of the AGN. The emission from stars is reduced in the *L*-band compared to that in the *K*-band, whereas hot ( $\sim 1000\text{K}$ ) dust heated by an AGN has strong emission at both *K* and *L*. In a starburst/AGN composite ULIRG, if the *L*-band emission were dominated by the AGN-powered hot dust emission, while the longer wavelength tail of the stellar emission extended to the shorter part of the *L*-band spectrum, then the *L*-band spectrum may appear to be concave. However, this scenario cannot produce the observed spectral gaps (point 1 above), so the detected features are ascribed to H<sub>2</sub>O ice absorption.

The shortest wavelength of the H<sub>2</sub>O ice absorption feature is  $\lambda_{\text{rest}} \sim 2.7 \mu\text{m}$  (Whittet et al. 1988; Smith et al. 1993). Due to redshifting, for the majority of the observed ULIRGs at  $z > 0.07$ , the continuum on the short-wavelength side of the absorption feature is included in our *L*-band spectra at  $\lambda_{\text{obs}} \sim 2.8\text{--}4.1 \mu\text{m}$ . Thus, continuum levels at both shorter and longer wavelength sides of important features (broad  $3.1 \mu\text{m}$  ice absorption,  $3.3 \mu\text{m}$  PAH emission, and  $3.4 \mu\text{m}$  absorption) are covered in our spectra, making continuum determination ambiguities small. To estimate the optical depth of this H<sub>2</sub>O absorption feature, we adopt a linear continuum, as we did for the  $3.4 \mu\text{m}$  absorption feature. Although Imanishi & Maloney (2003) adopted a concave quadratic continuum to derive the lower limits, linear continua are arguably more plausible, given that both the AGN and starburst components (outside the  $3.3 \mu\text{m}$  PAH emission feature) show linear continuum emission (Imanishi & Dudley 2000; Imanishi 2002, 2003; Imanishi & Wada 2004). This H<sub>2</sub>O ice absorption feature is spectrally very broad, and the continuum level can vary slightly, depending on the adopted data points used for the continuum determination. We tried several plausible linear continuum levels, and finally adopt the lowest plausible level to obtain a conservative lower limit for the optical depth of the  $3.1 \mu\text{m}$  H<sub>2</sub>O ice absorption feature ( $\tau_{3.1}$ ). The derived  $\tau_{3.1}$  values for ULIRGs showing this feature clearly are summarized in Table 4.

## 4.2. *K*-band spectra

Two ULIRGs, IRAS 08572+3915 and Mrk 1014, were observed with IRTF SpeX, and so *K*-band ( $\lambda=2.0\text{--}2.5 \mu\text{m}$ ) spectra were simultaneously taken. Figure 6 shows the *K*-band spectra of these two sources.

The *K*-band spectrum of IRAS 08572+3915 (Figure 6, *Left*) is similar to that presented

by Goldader et al. (1995). The spectrum is very red and displays no detectable CO absorption features due to stars at  $\lambda_{\text{rest}} > 2.29 \mu\text{m}$  or  $\lambda_{\text{obs}} > 2.43 \mu\text{m}$ , which suggests that featureless continuum emission from dust heated by an AGN dominates the  $K$ -band spectrum.

The  $K$ -band spectrum of Mrk 1014 (Figure 6, *Right*) shows a strong Pa $\alpha$  emission line. The emission line displays both broad and narrow components, as expected from the optical classification of this galaxy as Sy 1. The broad component has a line width of FWHM  $\sim 3100 \text{ km s}^{-1}$  and a flux of  $5 \times 10^{-14} \text{ ergs s}^{-1} \text{ cm}^{-2}$ . The narrow component has a line width of FWHM  $\sim 600 \text{ km s}^{-1}$  and a flux of  $1 \times 10^{-14} \text{ ergs s}^{-1} \text{ cm}^{-2}$ .

## 5. Discussion

In this section, we first focus on the investigations of the energy sources of non-Seyfert ULIRGs based on our  $L$ -band spectra (§5.1–5.5), and then combine these spectra with data at other wavelengths and compare these sources with the properties of Seyfert ULIRGs (§5.6–5.8).

### 5.1. The detected modestly obscured starbursts

The detection of the  $3.3 \mu\text{m}$  PAH emission clearly indicates the presence of starbursts in the majority of ULIRGs. Since dust extinction in the  $L$ -band is about 0.06 times as large as in the optical  $V$ -band ( $\lambda = 0.6 \mu\text{m}$ ; Rieke & Lebofsky 1985; Lutz et al. 1996), the attenuation of  $3.3 \mu\text{m}$  PAH emission with dust extinction of  $A_V \sim 15 \text{ mag}$  is less than 1 mag. Thus, the observed  $3.3 \mu\text{m}$  PAH emission luminosities can be used to determine the absolute magnitudes of modestly obscured ( $A_V < 15 \text{ mag}$ ) starburst activity.

At  $\lambda_{\text{rest}} \sim 3.3 \mu\text{m}$ , Pf $\delta$  emission is present, superposed on the  $3.3 \mu\text{m}$  PAH emission. The relative contribution from this Pf $\delta$  emission line is expected to be the highest in Sy 1 ULIRGs, because: (1) broad components from the AGNs are unattenuated, and (2)  $3.3 \mu\text{m}$  PAH emission is weak compared to starburst-dominated ULIRGs. For the Sy 1 ULIRGs Mrk 1014 and IRAS 07599+6508, we can estimate the contamination by the Pf $\delta$  emission using the measured Pa $\alpha$  emission line fluxes (This paper; Taniguchi et al. 1994). For high-transition broad and narrow emission lines, such as Pa $\alpha$  and Pf $\delta$ , case-B is applicable (Rhee & Larkin 2000), and so we adopt a Pf $\delta$ -to-Pa $\alpha$  flux ratio of 0.023 (Wynn-Williams 1984). The estimated Pf $\delta$  fluxes, including both broad and narrow components, are more than a factor of 20 smaller than the measured  $3.3 \mu\text{m}$  PAH flux (Mrk 1014) or its upper limit (IRAS 07599+6508) in Table 3. For another Sy 1 ULIRG Mrk 231, we find that the Pf $\delta$

flux, estimated based on the  $\text{Br}\gamma$  ( $\lambda_{\text{rest}} = 2.17 \mu\text{m}$ ) flux (Goldader et al. 1995) and case-B ( $\text{Pf}\delta/\text{Br}\gamma = 0.26$ ; Wynn-Williams 1984), is a factor of  $>25$  smaller than the observed  $3.3 \mu\text{m}$  PAH flux (Table 3). For the remaining Sy 1 ULIRGs, we adopt a median quasar spectrum at  $\lambda_{\text{rest}} = 1.8\text{--}2.0 \mu\text{m}$  (Murphy et al. 1999) and an average spectral energy distribution of quasars at  $\lambda > 1 \mu\text{m}$  ( $F\nu \propto \nu^{-1.4}$ ; Neugebauer et al. 1987). Assuming case-B, we find that the equivalent width of the  $\text{Pf}\delta$  line is  $\sim 0.3 \text{ nm}$  for a typical Sy 1 source. For Sy 2 and non-Seyfert ULIRGs, the  $\text{Pf}\delta$  contaminations are expected to be much smaller than Sy 1 ULIRGs. Whenever  $\text{Pa}\alpha$  fluxes are available in the literature (Veilleux et al. 1997, 1999b), we confirm that the expected  $\text{Pf}\delta$  fluxes never exceed 10% of the observed  $3.3 \mu\text{m}$  PAH fluxes or their upper limits in Sy 2 and non-Seyfert ULIRGs. Thus, we can safely assume that  $\text{Pf}\delta$  contamination is insignificant for the excess component at  $\lambda_{\text{rest}} \sim 3.3 \mu\text{m}$ , which must be mostly ascribed to  $3.3 \mu\text{m}$  PAH emission (§4.1).

The observed  $3.3 \mu\text{m}$  PAH to infrared luminosity ratios ( $L_{3.3\text{PAH}}/L_{\text{IR}}$ ) are summarized in column 4 of Table 3. The ratios are factors of 2 to more than 10 times smaller than those found in lower luminosity, less-obscured starbursts ( $\sim 10^{-3}$ ; Mouri et al. 1990; Imanishi 2002). Since emission from the ULIRGs’ cores ( $<500 \text{ pc}$ ) is covered in our slit spectra, except for the nearest ULIRG Arp 220 ( $z = 0.018$ ), the small  $L_{3.3\text{PAH}}/L_{\text{IR}}$  ratios suggest that the detected *nuclear* starbursts can account for only a small fraction of the infrared luminosities of the observed ULIRGs. Fischer (2000) have previously found that the  $6.2 \mu\text{m}$  PAH to infrared luminosity ratios in ULIRGs are smaller by a similar factor than in less-obscured starburst galaxies. The  $6.2 \mu\text{m}$  PAH luminosities were measured with the large apertures of *ISO*, and yet they show a similar PAH deficit: this indicates that PAH emission from the host galaxies, outside our slit spectra, is not energetically important in the infrared luminosities of ULIRGs (Soifer et al. 2000). Both the detected  $3.3 \mu\text{m}$  and  $6.2 \mu\text{m}$  PAH emission probe modestly obscured ( $A_V < 15 \text{ mag}$  or so) starbursts, presumably at the outer regions of the ULIRGs’ cores. The energy sources responsible for the bulk of the infrared emission of these ULIRGs must be deeply buried ( $A_V \gg 15 \text{ mag}$ ).

## 5.2. Buried AGNs with very weak starbursts

The energetically dominant, deeply buried energy sources at the cores of non-Seyfert ULIRGs can be either buried AGNs or very compact starbursts or both. Since buried AGNs can produce large infrared dust emission luminosities, without PAH emission (see §1), the small observed  $L_{3.3\text{PAH}}/L_{\text{IR}}$  values are naturally explained. Very highly obscured starbursts can also explain the small observed  $L_{3.3\text{PAH}}/L_{\text{IR}}$  ratios, because flux attenuation of the  $3.3 \mu\text{m}$  PAH emission may be significant, while that of longer wavelength infrared emission (8–

1000  $\mu\text{m}$ ) may not. These two scenarios are difficult to differentiate based on the absolute luminosities of PAH emission, but can be distinguished by the *equivalent width* of emission or absorption features. In a pure normal starburst, where HII regions, molecular gas, and photo-dissociation regions are spatially mixed, the equivalent width of the 3.3  $\mu\text{m}$  PAH emission feature is less affected by dust extinction (§1), and so the observed value should be close to the intrinsic one ( $\text{EW}_{3.3\text{PAH}} \sim 100 \text{ nm}$ ; Moorwood 1986; Imanishi & Dudley 2000), regardless of dust extinction of the starburst. On the other hand, an AGN produces a PAH-free featureless continuum, with strong absorption features when the AGN is highly dust-obscured. If this emission contributes significantly to an observed  $L$ -band flux, then the  $\text{EW}_{3.3\text{PAH}}$  value should be smaller than in normal starburst galaxies. The  $\text{EW}_{3.3\text{PAH}}$  values in starbursts have an average value of  $\text{EW}_{3.3\text{PAH}} \sim 100 \text{ nm}$ , with some scatter, but never become lower than 40 nm (Moorwood 1986). Thus, if we adopt  $\text{EW}_{3.3\text{PAH}} \lesssim 40 \text{ nm}$  as strong signatures of a significant contribution from the AGN’s PAH-free continuum, then we can argue that the three LINER ULIRGs IRAS 08572+3915NW, 12127–1412NE, and 17044+6720 possess powerful AGNs. All of them display strong dust absorption features at 3.1  $\mu\text{m}$  and/or 3.4  $\mu\text{m}$ , suggesting that the AGNs are deeply buried.

Kim et al. (2002) estimated the nuclear  $K'$ -band magnitudes within the central 4 kpc diameter ( $K'_4$ ) for the ULIRGs in the IRAS 1 Jy sample (their Table 3). We combine these data with the  $L$ -band magnitudes derived from our slit spectra ( $L_{\text{spec}}$ ), and find that the  $K'_4 - L_{\text{spec}}$  colors of the three ULIRGs, IRAS 08572+3915NW, 12127–1412NE, and 17044+6720, occupy the largest (reddest) three values. Hot dust emission heated by an AGN produces redder  $K - L$  colors than normal stellar emission and so the  $K - L$  colors of AGNs are usually redder than starbursts (Willner et al. 1984; Alonso-Herrero et al. 2003; Imanishi & Alonso-Herrero 2004; Imanishi & Wada 2004). The red  $K'_4 - L_{\text{spec}}$  colors again support the scenario that powerful buried AGNs are present and produce strong hot dust emission in these ULIRGs.

### 5.3. Buried AGNs with coexisting strong starbursts

Based on the  $\text{EW}_{3.3\text{PAH}}$  values, the presence of buried AGNs is strongly indicated in the three LINER ULIRGs discussed above. This was possible primarily because the 3.3  $\mu\text{m}$  PAH emission expected from starbursts is exceptionally weak in these ULIRGs. Hence these ULIRGs may be classified as almost pure buried AGNs. However, the nuclei of ULIRGs are generally extremely rich in molecular gas (Sanders & Mirabel 1996), which not only fuels the existing supermassive black holes and thereby increases the luminosities of AGNs, but is also likely to fuel star formation. Hence it is expected that, if powerful AGNs are present

in the majority of non-Seyfert ULIRGs, they will coexist with starbursts. It is therefore important to look for the signatures of powerful buried AGNs in the cores of starburst-containing ULIRGs. To detect the AGN signatures in these composite cores requires more careful analysis of the spectra than for the almost pure buried AGNs (Imanishi et al. 2001; Soifer et al. 2002; Imanishi & Maloney 2003; Spoon et al. 2004). Even if the intrinsic luminosities of a buried AGN and surrounding less-obscured starbursts are similar, the flux from the buried AGN will be more highly attenuated by dust extinction. In addition to this extinction, when the broad 3.1  $\mu\text{m}$  H<sub>2</sub>O ice absorption feature is present (Spoon et al. 2000; Imanishi & Maloney 2003), the AGN flux is suppressed even more severely. In this case, the 3.3  $\mu\text{m}$  PAH emission is not diluted significantly by the PAH-free continuum produced by the AGN, and so the small EW<sub>3.3PAH</sub> diagnostic can no longer be used.

To determine whether the remaining ULIRGs' cores consist of (a) modestly obscured starbursts and deeply buried *starbursts*, or of (b) modestly obscured starbursts and deeply buried *AGNs*, we use the absolute optical depth values of dust absorption features found in the *L*-band spectra. As mentioned in §1, these values can be used to distinguish whether the energy sources are spatially well mixed with dust, or are more centrally concentrated than the dust. Here we discuss this point more quantitatively.

In a mixed dust/source geometry, flux attenuation as a function of optical depth is

$$I(\tau_\lambda) = I_0 \times \frac{1 - e^{-\tau_\lambda}}{\tau_\lambda}, \quad (1)$$

where  $I_0$  is the unattenuated intrinsic flux and  $\tau_\lambda$  is the optical depth at each wavelength; this takes different values inside and outside the absorption features. The 3.1  $\mu\text{m}$  H<sub>2</sub>O ice absorption feature is observed if dust grains are located deep inside molecular gas, are shielded from ambient UV radiation, and are covered with an ice mantle (Whittet et al. 1988). The feature is not observed in the diffuse interstellar medium outside molecular clouds, since ice mantles cannot survive exposure to the ambient UV radiation. Thus, its optical depth reflects the total column density of ice-covered dust grains in molecular gas, in front of the continuum-emitting energy sources. The observed optical depth of the 3.1  $\mu\text{m}$  H<sub>2</sub>O ice absorption feature is, by definition, dependent on the difference of flux attenuation between the ice absorption feature and the 3–4  $\mu\text{m}$  continuum outside the feature. Imanishi & Maloney (2003) have shown that, in a mixed dust/source geometry,

$$\tau_{3.1} \equiv \ln\left[\frac{1 - e^{-\tau_{cont}}}{\tau_{cont}} \times \frac{\tau_{ice}}{1 - e^{-\tau_{ice}}}\right] \quad (2)$$

$$= \ln\left[(1 + f) \frac{1 - e^{-0.06 \times A_V}}{1 - e^{-0.06 \times A_V \times (1+f)}}\right], \quad (3)$$

where  $f$  is the fraction of dust that is covered with an ice mantle, and it is assumed that the  $\tau_{3.1}/A_V$  ratio (the abundance of H<sub>2</sub>O ice relative to dust grains in the regions where an

ice mantle can survive) is similar to that in Galactic molecular clouds (Smith et al. 1993; Tanaka et al. 1990; Murakawa et al. 2000).

Stars are formed within the high density cores of molecular clouds. If we observe such molecular clouds individually, then the energy sources should be more centrally concentrated than the gas and accompanying dust. However, starburst galaxies consist of many such stars and the energy sources will be distributed throughout the volume of the starburst (Soifer et al. 2000; Siebenmorgen et al. 2004). Hence for observations of entire starburst nuclei, the stellar energy sources and dust will be relatively well mixed spatially (Figure 7a). In fact, detailed studies of the prototypical starburst galaxy M82 strongly suggest that the stars of the burst and the obscuring dust are spatially well mixed (Puxley 1991; McLeod et al. 1993; Forster Schreiber et al. 2001). Thus, it seems quite reasonable to regard that starbursts can be represented by this mixed dust/source geometry model.

The observed  $\tau_{3.1}$  depends on  $A_V$  and the  $f$ -value, the fraction of dust that is covered with an ice mantle. If we assume that the  $f$  values at the cores of ULIRGs are similar to that in the well-studied prototype starburst galaxy M82 ( $f \sim 30\%$ ; Imanishi & Maloney 2003), then  $\tau_{3.1}$  will be  $< 0.3$  for any  $A_V$  value in a mixed dust/source geometry (Imanishi & Maloney 2003). In reality, the cores of ULIRGs are estimated to have much higher surface brightnesses than M82 (Soifer et al. 2000), implying a much larger ambient radiation field. In a mixed dust/source geometry, the radiation environment in the cores of ULIRGs will therefore be much harsher and it will be much more difficult for ice mantles to survive than in M82. In this geometry, the  $f$ -values in ULIRGs' cores must be smaller than the assumed value of  $f = 30\%$ , and thus the upper limit of  $\tau_{3.1} = 0.3$  should be robust.

On the other hand, in a buried AGN, the energy source is very compact and is more centrally concentrated than the surrounding dust (Figure 7b, *Left*). In this geometry, a simple foreground screen dust model is applicable and the flux attenuation is

$$I(\tau_\lambda) = I_0 \times e^{-\tau_\lambda}. \quad (4)$$

The  $\tau_{3.1}$  value is expressed as

$$\tau_{3.1} \equiv \ln \frac{e^{-\tau_{cont}}}{e^{-\tau_{ice}}} \quad (5)$$

$$= \ln \frac{e^{-0.06 \times A_V}}{e^{-0.06 \times A_V \times (1+f)}} \quad (6)$$

$$= 0.06 \times A_V \times f. \quad (7)$$

$$(8)$$

The  $\tau_{3.1}$  value can become arbitrarily large with increasing  $A_V$  provided  $f$  is non-zero. In this centrally-concentrated energy-source geometry, once the shielding column density of

dust and molecular gas around the central energy source becomes sufficiently large, dust grains at a given distance from the center can be covered with ice mantles ( $f > 0$ ), and so a large  $\tau_{3.1}$  value can be produced. Therefore, observing larger  $\tau_{3.1}$  values than the limit for a mixed dust/source geometry (0.3) is another independent means to determine the geometry of ULIRGs' cores, and therefore the nature of the central energy sources.

Aside from the three LINER ULIRGs with strong buried AGN signatures discussed above (IRAS 08572+3915NW, 12127–1412NE, and 17044+6720), 14 LINER, 3 HII, and 2 optically-unclassified ULIRGs' nuclei have observed  $\tau_{3.1}$  values larger than the threshold (Table 4). Note that these observed values are contaminated by weakly obscured starburst emission. Hence these observed optical depths provide only lower limits to the true  $\tau_{3.1}$  values for the central buried energy sources. For these ULIRGs' nuclei, a centrally-concentrated energy-source geometry provides a natural explanation for the large observed  $\tau_{3.1}$  values.

There is one case in which a mixed dust/source geometry for the cores can exceed the threshold value of 0.3. If the host galaxies are viewed close to edge-on and a large column density of ice-covered dust is present in the interstellar medium of the host galaxies, exterior to the starburst core, then a foreground screen model is applicable and  $\tau_{3.1}$  can be large, just as for a centrally-concentrated energy source. However, the presence of ice-covered dust requires that the dust be located deep inside molecular gas (Whittet et al. 1988). Strong 3.1  $\mu\text{m}$  H<sub>2</sub>O ice absorption is found in the dense cores of molecular gas (Murakawa et al. 2000), and such dense molecular gas, probed by e.g., HCN ( $J = 1-0$ ) emission at  $\nu = 88.632$  GHz ( $\lambda = 3.3848$  mm) in the millimeter wavelength range, is normally seen only in the nuclei of ULIRGs (Imanishi, Nakanishi, & Kohno 2005, in preparation). It is thus very likely that the strong observed H<sub>2</sub>O ice absorption largely arises in the cores of the ULIRGs rather than in the extended interstellar medium of the host galaxies. The large observed H<sub>2</sub>O ice absorption optical depths can thus be taken as some evidence of a centrally-concentrated energy source geometry at the cores of these ULIRGs.

Soifer et al. (2000) studied the cores of seven nearby ULIRGs and estimated that, in the majority (six out of seven) of these ULIRGs' cores, the emission surface brightnesses are very high ( $\sim 10^{13} L_{\odot} \text{ kpc}^{-2}$ ) and close to the maximum observed values seen in the cores of Galactic HII regions, even if the energy sources are uniformly distributed over the cores ( $< 500$  pc in size). Provided that the emission properties of the six ULIRGs' cores (Soifer et al. 2000) are representative of the majority of nearby ULIRGs, surface brightnesses of the *centrally-concentrated* energy sources would be even higher, making *exceptionally centrally-concentrated starbursts* less likely, if not completely ruled out. AGNs are more natural explanations for the centrally-concentrated high surface brightness energy sources at the cores of ULIRGs. We thus take the centrally-concentrated energy sources as *tentative* evidence for



buried AGNs.

We can apply the same argument concerning the geometry of the energy sources and dust to the absolute optical depth of the  $3.4 \mu\text{m}$  carbonaceous dust absorption feature ( $\tau_{3.4}$ ). This absorption feature is found if a source is obscured by bare dust grains (Pendleton et al. 1994; Imanishi et al. 1996; Rawlings et al. 2003), but absent if the absorbing dust is ice-covered (Mennella et al. 2001). Thus, the optical depth of the  $3.4 \mu\text{m}$  absorption feature traces the column density of bare carbonaceous dust grains. Imanishi & Maloney (2003) have quantitatively demonstrated that  $\tau_{3.4}$  cannot be larger than 0.2 in a mixed dust/source geometry. Two LINER ULIRGs, IRAS 08572+3915NW and IRAS 12127–1412NE, show  $\tau_{3.4} > 0.2$  (Table 4). These ULIRGs have already been classified as buried AGNs based on their  $\text{EW}_{3.3\text{PAH}}$  values (§5.2). For them, additional support for powerful buried AGNs is provided here from the geometry implied by the depth of their  $3.4 \mu\text{m}$  absorption features.

For the remaining ULIRGs where (1) the  $\text{EW}_{3.3\text{PAH}}$  values are in the possible scattered range of starburst galaxies ( $>40 \text{ nm}$ ), and (2) no strong dust absorption features are observed, there are no obvious signatures of buried AGNs. Their spectra can be explained by either of the following scenarios: (1) the cores are dominated by starbursts with a mixed dust/source geometry, or (2) the cores do possess powerful buried AGNs, but the emission from the AGNs is so highly attenuated that its contribution to the observed  $L$ -band fluxes is not significant. We have no way to distinguish between these two scenarios, and their energy sources remain undetermined by our  $L$ -band spectroscopic method. There are some known examples (e.g., NGC 4418) which show no obvious buried AGN signatures in the  $L$ -band spectra (Imanishi et al. 2004), but almost certainly contain powerful AGNs based on longer wavelength data (Dudley & Wynn-Williams 1997; Spoon et al. 2001). Observations at wavelengths with lower dust extinction are necessary to unveil possible buried AGNs which are undetectable even in the  $L$ -band.

#### 5.4. Dust Extinction and Dereddened AGN luminosities

In a centrally-concentrated energy source geometry, dust at a temperature of 1000 K, which is close to the innermost dust sublimation radius, produces emission with a peak at  $\lambda \sim 3 \mu\text{m}$  (Figure 7b, *Right*), assuming approximately blackbody emission. Dust grains at larger radii, with lower temperatures, show emission peaks at longer infrared wavelengths. The dust extinction toward the  $3 \mu\text{m}$  continuum-emitting region,  $A_V(3\mu\text{m})$ , can be estimated from the  $\tau_{3.4}$  (bare dust) and  $\tau_{3.1}$  (ice-covered dust) values, and can provide a better estimate for dust extinction toward the buried AGN itself than the estimate using longer infrared wavelengths, which only probes dust extinction toward the outer, cooler emission regions

(Figure 7b, *Right*). If we assume that the optical depth of these dust absorption features, relative to  $A_V$ , is similar to the Galactic diffuse interstellar medium ( $\tau_{3.4}/A_V = 0.004\text{--}0.007$ ; Pendleton et al. 1994,  $\tau_{3.1}/A_V = 0.06$ ; Smith et al. 1993; Tanaka et al. 1990; Murakawa et al. 2000), and if we adopt a foreground screen model which should be applicable to the centrally-concentrated energy source geometry, then the estimated  $A_V$  values are summarized in column 4 of Table 4.

For the three ULIRGs with very small  $EW_{3.3\text{PAH}}$  values, IRAS 08572+3915NW, 12127–1412NE, and IRAS 17044+6720, the  $L$ -band emission is concluded to predominantly come from hot dust emission heated by the buried AGN. We can estimate the dereddened luminosity of the AGN-heated dust emission fairly straightforwardly for these sources. Assuming that dust extinction at  $L$ , relative to  $V$ , is similar to the Galactic diffuse interstellar medium ( $A_L/A_V \sim 0.06$ ; Rieke & Lebofsky 1985; Lutz et al. 1996), the dereddened AGN luminosities at  $\lambda_{\text{rest}} = 3\text{--}4 \mu\text{m}$  are  $>50$ ,  $>10$ , and  $0.7\text{--}2 \times 10^{45} \text{ ergs s}^{-1}$ , respectively, for IRAS 08572+3915NW, 12127–1412NE, and 17044+6720. The dereddened AGN luminosities could quantitatively account for the bulk of the infrared luminosities of these ULIRGs ( $L_{\text{IR}} \sim 5 \times 10^{45} \text{ ergs s}^{-1}$ ). For IRAS 08572+3915NW and 12127–1412NE, the dereddened AGN luminosities significantly exceed the observed infrared luminosities. A similar excess was found in the ULIRG Superantennae (Risaliti et al. 2003), and the excess implies that the  $\tau_{3.4}/A_L$  ratios in some ULIRGs’ cores are larger than the ratios found in the Galactic interstellar medium.

For the remaining starburst/buried-AGN composite ULIRGs (large  $EW_{3.3\text{PAH}}$  values with  $>40 \text{ nm}$  and strong  $3.1 \mu\text{m}$   $\text{H}_2\text{O}$  ice absorption with  $\tau_{3.1} > 0.3$ ), no detectable  $3.4 \mu\text{m}$  absorption features are found. The optical depths of the  $3.1 \mu\text{m}$  and  $3.4 \mu\text{m}$  absorption features probe the column density of ice-covered and bare dust grains, respectively, but it seems strange that there are no bare dust grains in the nuclear regions of these ULIRGs. The  $3.3 \mu\text{m}$  PAH emission feature is often accompanied by a sub-peak at  $3.4 \mu\text{m}$  (Tokunaga et al. 1991; Imanishi & Dudley 2000) and this sub-peak may dilute the  $3.4 \mu\text{m}$  dust absorption feature at the same wavelength. In fact, some ULIRGs’ spectra with strong  $3.3 \mu\text{m}$  PAH emission show sub-peaks at  $\lambda_{\text{rest}} = 3.4 \mu\text{m}$  in Figures 1, 2, and 3 (e.g., IRAS 09039+0503, 13509+0442, and 14197+0813). For those ULIRGs with  $EW_{3.3\text{PAH}} > 40 \text{ nm}$ , the estimated  $A_V$  values (Table 4, column 4) should be taken as only lower limits for dust extinction toward the inner  $3 \mu\text{m}$  continuum emitting regions at the cores. Although quantitative values are highly uncertain for these sources, the cores are usually assumed to dominate the infrared luminosities of nearby ULIRGs (Soifer et al. 2000), and the cores of these composite ULIRGs are suggested to have centrally-concentrated energy sources, most likely buried AGNs. Thus, the buried AGNs in these ULIRGs could account for the bulk of their observed infrared luminosities.

### 5.5. Dependence on optical spectral type

In total,  $L$ -band spectra of 27 LINER and 13 HII ULIRGs’ nuclei have been obtained. 3 LINER ULIRGs’ and no HII ULIRGs’ nuclei show clear evidence for almost pure buried AGNs (§5.2). Additionally, 14 LINER and 3 HII ULIRGs’ nuclei have tentative evidence for powerful buried AGNs, in addition to modestly obscured starbursts (§5.3). Combining these values, 17 out of 27 LINER ULIRGs’ nuclei (63%) and 3 out of 13 HII ULIRGs (23%) display some degree of evidence for powerful buried AGNs. The observed LINER ULIRGs comprise a complete sample (§2). The observed HII ULIRGs also constitute a complete sample in the right ascension range 10–22 hr (§2). The fraction of sources with signatures of buried AGNs is significantly higher in LINER ULIRGs than HII ULIRGs. This suggests that a larger fraction of LINER ULIRGs may have powerful buried AGNs than HII ULIRGs.

Some ULIRGs have spectra of poor signal-to-noise ratios, and the presence of strong dust absorption features at  $3.1\ \mu\text{m}$  ( $\tau_{3.1} > 0.3$ ) or  $3.4\ \mu\text{m}$  ( $\tau_{3.4} > 0.2$ ) may be missed. Strong  $3.1\ \mu\text{m}$  H<sub>2</sub>O ice absorption may be present, but be missed due to poor signal-to-noise ratios, in four LINER ULIRGs’ nuclei (IRAS 12112+0305NE, 12112+0305SW, 14252–1550W, and 16468+5200E) in Figure 1, and one HII ULIRG’s nucleus (IRAS 21208–0519N) in Figure 2. The two LINER ULIRGs (IRAS 10485–1447 and 16090–0139) may have large  $\tau_{3.4}$  values. Even if only the HII ULIRG IRAS 21208–0519N is included as sources with tentative buried AGN signatures, the AGN fraction in HII ULIRGs’ nuclei is only 31% (4/13), significantly below the fraction for LINER ULIRGs’ nuclei.

In a pure buried AGN, X-ray dissociation regions (XDRs), dominated by low-ionization species (Maloney et al. 1996), should develop and a LINER-type optical spectrum is expected (Imanishi et al. 2001), rather than a typical Seyfert spectrum originating in the narrow line regions (NLRs). The discovery of pure powerful buried AGNs with no detectable starbursts in the two LINER ULIRGs (IRAS 08572+3915NW and 12127–1412NE) may be explained by this scenario.

For the remaining LINER ULIRGs with coexisting modestly-obscured starbursts, the LINER optical spectra can be due to XDRs and/or shocks driven by the starbursts (Taniguchi et al. 1999; Lutz et al. 1999). In the case of XDRs, even though the central AGN itself is deeply buried, emission from the surrounding XDRs can be relatively unobscured. Although the origin of the LINER optical spectra in these ULIRGs is unclear, the higher detection rate of powerful buried AGNs in LINER ULIRGs suggests that emission from XDRs may be important in the optical.

### 5.6. Comparison with VLA radio observations

Nagar et al. (2003) performed VLA observations at  $\nu = 15$  GHz ( $\lambda = 2$  cm), with 150 mas spatial resolution, of a large sample of ULIRGs in the same IRAS 1 Jy sample, and searched for compact radio core emission, another good indicator of an AGN. They concluded that the detection rate of the radio cores in LINER ULIRGs ( $\sim 74\%$ ) was substantially higher than in HII ULIRGs ( $\sim 14\%$ ). Our higher detection rate of buried AGN signatures in LINER ULIRGs than in HII ULIRGs is both qualitatively and quantitatively similar to their conclusion.

Table 3 (columns 6 and 7) summarizes information on which individual ULIRGs have detectable (or non-detectable) radio cores (Nagar et al. 2003), in comparison with the buried AGN signatures from our  $L$ -band spectroscopic method. Among the three ULIRGs with clear buried AGN signatures, two sources, IRAS 08572+3915NW and 17044+6720, were observed with VLA and both (100% = 2/2) show core radio emission. For ULIRGs with tentative evidence for buried AGNs, 8 LINER, 3 HII, and 1 optically-unclassified ULIRGs' nuclei have VLA data, and 5 LINER, 2 HII, and 1 unclassified ULIRGs' nuclei have detectable VLA radio cores. Hence the detection rate is 67 %  $\{= (5+2+1)/(8+3+1)\}$ . For ULIRGs without buried AGN signatures in the  $L$ -band spectra, VLA cores were detected in 8 out of 17 sources (47 %). The higher detection rate of the VLA cores in ULIRGs that show a higher level of buried AGN evidence in the  $L$ -band suggest that our  $L$ -band spectroscopic method is a reliable, if not perfect, tracer of elusive buried AGNs in non-Seyfert ULIRGs.

Our infrared  $L$ -band spectra can probe dust emission heated by an AGN and thus quantitatively determine the dust emission luminosity, the dominant emission mechanism of ULIRGs. However, the spectra may miss the AGN signatures if the AGN emission is highly attenuated by dust extinction. On the other hand, the radio observations are negligibly affected by dust extinction, and so could detect highly dust-obscured AGNs that may be missed in our  $L$ -band spectroscopic method. However, the radio data trace synchrotron emission and may not be proportional to ULIRGs' dust emission luminosities (Nagar et al. 2003). Thus, the infrared  $L$ -band and radio observations are complementary to each other. The fact that both independent methods provide a similar result suggests that the higher detection rate of powerful buried AGNs in LINER ULIRGs than HII ULIRGs is probably real.

### 5.7. Comparison with Seyfert ULIRGs

We compare the  $L$ -band spectral properties of non-Seyfert ULIRGs showing buried AGN signatures, with those of Seyfert ULIRGs (i.e., known AGN-possessing ULIRGs). The

apparent main difference between them is that the ionizing radiation from the putative AGNs in non-Seyfert ULIRGs is obscured by the surrounding dust along virtually all lines-of-sight, while dust around the AGNs in Seyfert ULIRGs is distributed in a “torus”, and ionizing radiation from the AGNs can escape along the torus axis, allowing the Seyfert signatures to be detectable in the optical. In Table 3, all Seyfert ULIRGs’ nuclei show  $EW_{3.3PAH}$  smaller than  $\sim 40$  nm. The  $EW_{3.3PAH}$  values of Sy 1 ULIRGs are systematically smaller than Sy 2 ULIRGs, which is reasonable because unattenuated emission from unobscured AGNs in Sy 1 ULIRGs can reduce the  $EW_{3.3PAH}$  values more strongly than attenuated emission from obscured AGNs in Sy 2 ULIRGs. In Sy 2 ULIRGs, the significantly smaller  $EW_{3.3PAH}$  values than seen in starburst galaxies suggest that the strong dilution of the PAH emission by the PAH-free continuum produced by the AGN is present. Our  $L$ -band spectroscopic method has succeeded in detecting obscured AGN signatures in all of the known obscured-AGN-possessing Sy 2 ULIRGs observed, demonstrating that this method is very effective.

Among the eight Sy 2 ULIRGs’ nuclei, Nagar et al. (2003) presented VLA data for four sources, and three sources show core emission (Table 3). The VLA core detection rate is 75% (3/4). For the seven Sy 1 ULIRGs’ nuclei observed by us, five sources have VLA data and all show radio core emission (100% = 5/5; Table 3). These detection rates are again clearly higher than those for ULIRGs with no obvious AGN signatures in our  $L$ -band spectra.

Figure 8(a) plots the  $L_{3.3PAH}/L_{IR}$  ratios of ULIRGs, separated by optical spectral types. Both non-Seyfert and Seyfert ULIRGs are plotted. The median  $L_{3.3PAH}/L_{IR}$  values are 0.1 (LINER), 0.2 (HII), 0.09 (Sy 2) and  $<0.15$  (Sy 1). The  $L_{3.3PAH}/L_{IR}$  ratios do not differ significantly between non-Seyfert and Seyfert ULIRGs, suggesting that both types of ULIRGs possess detectable modestly-obscured starburst activity with similar absolute luminosities.

Figure 8(b) plots the rest-frame equivalent widths of the  $3.3 \mu\text{m}$  PAH emission ( $EW_{3.3PAH}$ ), separated by optical spectral types. In this plot, Sy 2 ULIRGs tend to show smaller  $EW_{3.3PAH}$  values than non-Seyfert ULIRGs, while Sy 1 ULIRGs show the smallest values. The median  $EW_{3.3PAH}$  values are 75 nm (LINER), 85 nm (HII), 15 nm (Sy 2) and  $<4$  nm (Sy 1). Even though the absolute luminosities of the detectable modestly-obscured starbursts are similar, less-obscured AGNs can have a larger contribution to the observed  $L$ -band flux, and thereby decrease the  $EW_{3.3PAH}$  values. The trends in Figure 8(a) and (b) can be explained by a scenario where AGNs in Sy 2 ULIRGs tend to be less obscured by dust along our line-of-sight than AGNs in non-Seyfert ULIRGs. In fact, while many non-Seyfert ULIRGs show clear absorption features at  $3.1 \mu\text{m}$  by  $\text{H}_2\text{O}$  ice and at  $3.4 \mu\text{m}$  by bare carbonaceous dust grains (Figure 1, 2, 3), no such absorption features are found in the  $L$ -band spectra of Sy 2 ULIRGs, with the exception of IRAS 12072–0444N (Figure 4), supporting the less-obscuration scenario for AGNs in Sy 2 ULIRGs. We argue that buried AGNs in non-Seyfert ULIRGs and

optically visible AGNs (obscured by torus-shaped dust) in Sy 2 ULIRGs are different not only in the dust geometry, but also in the dust column density along our line-of-sight, in that the dust columns toward the AGNs in non-Seyfert ULIRGs are much higher. Since the dust covering factor around buried AGNs in non-Seyfert ULIRGs (almost all directions) is also larger than AGNs in Sy 2 ULIRGs (torus-shaped), the total amount of nuclear dust must be larger in the former. The optical (non-)detectability of Seyfert signatures in ULIRGs depends not on the presence or absence of powerful AGNs, but largely on the mass of gas and dust in the nuclei.

### 5.8. Dependence on far-infrared colors

Based on the *IRAS* 25  $\mu\text{m}$  to 60  $\mu\text{m}$  flux ratio ( $f_{25}/f_{60}$ ), ULIRGs are divided into warm ( $> 0.2$ ) and cool ( $< 0.2$ ) sources (Sanders et al. 1988). The majority of non-Seyfert ULIRGs show cool far-infrared colors (Table 1). Optical spectroscopy of galaxies with warm far-infrared colors often reveals Seyfert signatures (de Grijp et al. 1987; Keel et al. 2005), while starburst galaxies usually show cool far-infrared colors. The warm colors of galaxies showing optical Seyfert signatures are usually interpreted as emission from dust in the close vicinity of an AGN, whose temperature can be higher than that in starbursts, because of the higher radiation density in the former. It is sometimes argued that cool components of the far-infrared emission from ULIRGs must be starburst-dominated (e.g., Downes & Solomon 1998). However, the far-infrared color from AGN-heated dust is highly dependent on the column density of dust around an AGN, in that a larger column density makes the far-infrared color cooler ( $f_{25}/f_{60}$  ratio smaller). Our *L*-band spectra suggest that buried AGNs in non-Seyfert ULIRGs are more highly dust obscured, and thus produce cooler far-infrared colors than AGNs in Sy 2 ULIRGs.

Figure 9(a) compares the observed 3.3  $\mu\text{m}$  PAH to infrared luminosity ratios, with *IRAS* 25  $\mu\text{m}$  to 60  $\mu\text{m}$  flux ratios (i.e., far-infrared color), for non-Seyfert ULIRGs. There is no clear trend. If the detected 3.3  $\mu\text{m}$  PAH emission only probes the modestly-obscured energetically-insignificant surface starbursts (§5.1), and buried energy sources are responsible for the infrared emission at 25  $\mu\text{m}$  and 60  $\mu\text{m}$ , no trend is expected.

Figure 9(b) compares the  $\text{EW}_{3.3\text{PAH}}$  and far-infrared colors for non-Seyfert ULIRGs. The three ULIRGs with almost pure buried AGNs, IRAS 08572+3915NW, 12127–1412NE, and 17044+6720, are distributed on the warm side, but IRAS 12127–1412NE has a cool far-infrared color. Thus, there is at least one example of a pure buried AGN that produces a cool far-infrared color. The bulk of ULIRGs with tentative evidence of buried AGNs are also classified as cool sources, and their far-infrared color distribution overlaps with the colors of

ULIRGs with no AGN signatures.

We next compare the properties of the two pure buried AGNs, IRAS 08572+3915NW and 12127–1412NE. IRAS 08572+3915NW shows only 3.4  $\mu\text{m}$  dust absorption feature, with no detectable 3.1  $\mu\text{m}$  H<sub>2</sub>O ice absorption. Assuming Galactic dust properties,  $A_V > 110$  mag is estimated toward the inner 3  $\mu\text{m}$  continuum emitting regions, close to the central AGN. On the other hand, the bare dust column of IRAS 12127–1412NE ( $\tau_{3.4} = 0.35$ ) is estimated to be  $A_V > 50$  mag. This source displays ice absorption ( $\tau_{3.1}$ ), and the column of ice-covered dust is estimated to be  $A_V > 6$  mag. The total dust column in IRAS 08572+3915NW may be higher than IRAS 12127–1412NE, and yet the former source shows a warmer infrared color. This apparently contradicts the simple prediction that the far-infrared color is cooler when a larger amount of dust obscures an AGN, assuming the dust properties are similar. However, IRAS 08572+3915NW and 12127–1412NE are different in that strong ice absorption is found only in the latter source. Ice-covered dust grains can make a cooler far-infrared color (smaller  $f_{25}/f_{60}$  ratio) than do bare dust grains, because of the change of optical constants in the infrared (Dudley et al. 2003). The cooler color of IRAS 12127–1412NE than 08572+3915NW may be due to the presence of a significant amount of ice.

## 6. Summary

We presented the results of infrared  $L$ -band (3–4  $\mu\text{m}$ ) slit spectroscopy of the nuclei of a large sample of nearby ULIRGs in the IRAS 1 Jy sample. ULIRGs with no obvious Seyfert signatures in the optical (i.e., LINER, HII, and unclassified) were mainly observed and spectra of 27 LINER, 13 HII, and 2 optically-unclassified ULIRGs’ nuclei were obtained. Using the 3.3  $\mu\text{m}$  PAH emission, 3.1  $\mu\text{m}$  H<sub>2</sub>O ice absorption and 3.4  $\mu\text{m}$  carbonaceous dust absorption features, we investigated whether the cores of these ULIRGs can be explained by very compact starbursts only, or show signatures of buried AGNs. Since our spectra covered both the shorter and longer wavelength sides of these features, we were able to distinguish between absorption-dominated and emission-dominated sources with small ambiguities. These spectra were compared with known AGN-possessing ULIRGs’ nuclei (8 Sy 2 and 7 Sy 1) and we found the following main conclusions.

1. The 3.3  $\mu\text{m}$  PAH emission, the probe of starbursts, was detected in all but two non-Seyfert ULIRGs. It is likely that modestly-obscured ( $A_V < 15$  mag) starbursts at the surface of ULIRGs’ cores are responsible for the detected PAH emission. The observed 3.3  $\mu\text{m}$  PAH to infrared luminosity ratios were smaller by a factor of 2 to  $>10$  than those found in less infrared-luminous starbursts, suggesting that the detected modestly-obscured starbursts are energetically insignificant.

2. Three LINER ULIRGs, IRAS 08572+3915NW, 12127–1412NE, and 17044+6720, showed 3.3  $\mu\text{m}$  PAH emission equivalent widths substantially smaller than typical values found in starburst galaxies. These ULIRGs were classified as sources dominated by almost pure buried AGNs, with no detectable or very weak starburst activity.
3. Besides these three ULIRGs, the absolute optical depths of 3.1  $\mu\text{m}$  H<sub>2</sub>O ice absorption feature were used to distinguish whether the energy sources at the cores of ULIRGs are more centrally concentrated than the surrounding dust (as is expected for a buried AGN), or are spatially well mixed with dust (a normal starburst). The large optical depths in 14 LINER, 3 HII, and 2 unclassified ULIRGs’ nuclei suggested that the energy sources are more centrally concentrated than the surrounding dust, unless a large amount of foreground ice-covered dust is present in the interstellar medium of the host galaxies, which we consider unlikely. These ULIRGs were classified as showing tentative evidence for powerful buried AGNs.
4. Based on the optical depths of the 3.4  $\mu\text{m}$  carbonaceous dust absorption feature, centrally-concentrated energy sources were suggested in the two LINER ULIRGs, IRAS 08572+3915NW and 12127–1412NE. Both of them had already been classified as buried AGNs from the 3.3  $\mu\text{m}$  PAH equivalent widths, and thus powerful buried AGNs were consistently identified with two independent methods.
5. In total, 17 out of 27 (63%) LINER ULIRGs’ nuclei and 3 out of 13 HII ULIRGs’ nuclei (23%) showed some evidence for buried AGNs. The higher detection rate of buried AGNs in LINER ULIRGs than in HII ULIRGs was similar to the higher detection rate of compact radio cores (also a signature of AGNs) in the former.
6. *L*-band spectra of 8 Sy 2 and 7 Sy 1 ULIRGs’ nuclei were obtained, and the 3.3  $\mu\text{m}$  PAH emission was detected in 7 (out of 8) and 5 (out of 7) sources, respectively, suggesting that these Seyfert ULIRGs also contain detectable starburst activity.
7. Based on the equivalent widths of the 3.3  $\mu\text{m}$  PAH emission, our *L*-band spectra successfully detected AGN signatures in all of the observed Seyfert 2 ULIRGs (known-obscured-AGN-possessing ULIRGs), demonstrating that our *L*-band spectroscopic method is indeed effective in revealing signatures of obscured AGNs.
8. The detection rate of VLA radio cores was higher in ULIRGs that display evidence of buried AGNs in the *L*-band. This suggested that our *L*-band spectroscopic method is reliable, if not perfect.
9. Among 8 observed Sy 2 ULIRGs, only IRAS 12072–0444N showed a clear 3.4  $\mu\text{m}$  carbonaceous dust absorption feature. The remaining Sy 2 ULIRGs showed neither



detectable  $3.4 \mu\text{m}$  nor  $3.1 \mu\text{m}$  absorption features.

10. There was no systematic difference in the  $3.3 \mu\text{m}$  PAH to infrared luminosity ratios between Seyfert and non-Seyfert ULIRGs. However, Sy 1 and 2 ULIRGs tended to show smaller rest-frame equivalent widths of the  $3.3 \mu\text{m}$  PAH emission than non-Seyfert ULIRGs, with Sy 1 ULIRGs (unobscured AGNs) exhibiting the smallest values. The optical depths of absorption features in the  $L$ -band were also generally smaller in Sy 2 ULIRGs than in non-Seyfert ULIRGs. These results were naturally explained if AGNs in non-Seyfert ULIRGs are more highly obscured by dust along our sightline than the AGNs in Sy 2 ULIRGs.
11. Evidence for buried AGNs was found in non-Seyfert ULIRGs with both warm and cool far-infrared colors. The LINER ULIRG dominated by a pure buried AGN, IRAS 12127–1412NE, has a cool far-infrared color. The cool far-infrared color in this pure buried AGN could be the consequences of a large dust column density around an AGN, including ice-covered dust, as is implied from strong dust absorption features at  $3.1 \mu\text{m}$  and  $3.4 \mu\text{m}$ .
12. Our  $L$ -band spectroscopy revealed the presence of AGNs in many non-Seyfert ULIRGs, and these AGNs are thought to be obscured (at least opaque to the AGN’s ionizing radiation) along virtually all sightlines so as to be optically elusive (Maiolino et al. 2003). This dust geometry is fundamentally different from the AGNs in Sy 2 ULIRGs which are obscured by dust in a torus geometry. Together with the above finding that dust column along our line-of-sight is higher in AGNs in non-Seyfert ULIRGs, it was implied that a larger amount of dust is concentrated surrounding the AGNs at the nuclei of non-Seyfert ULIRGs than Seyfert ULIRGs. We argued that the (non-)detection of Seyfert signatures in the optical is highly dependent on the total amount of dust and its covering factor around a central AGN, and that many non-Seyfert ULIRGs may contain powerful buried AGNs. Other types of careful investigations at the wavelengths of lower dust extinction are important to find new buried AGNs which may even be undetectable in our  $L$ -band spectroscopic method.

We are grateful to H. Terada, M. Ishii, R. Potter, E. Pickett, A. Hatakeyama, B. Golisch, D. Griep, P. Sears for their support during our Subaru and IRTF observing runs. We thank the anonymous referee for his/her useful comments. M.I. is supported by Grants-in-Aid for Scientific Research (16740117). Research in Infrared Astronomy at the Naval Research Laboratory is supported by the Office of Naval Research (USA). Some part of the data analysis was made using a computer system operated by the Astronomical Data Analysis Center

(ADAC) and the Subaru Telescope of the National Astronomical Observatory, Japan. This research has made use of the SIMBAD database, operated at CDS, Strasbourg, France, and of the NASA/IPAC Extragalactic Database (NED) which is operated by the Jet Propulsion Laboratory, California Institute of Technology, under contract with the National Aeronautics and Space Administration.

## REFERENCES

- Alonso-Herrero, A., Quillen, A. C., Rieke, G. H., Ivanov, V., & Efstathiou, A. 2003, *AJ*, 126, 81
- Antonucci, R. 1993, *ARA&A*, 31, 473
- Armus, L., et al. 2004, *ApJS*, 154, 178
- Blain, A. W., Smail, I., Ivison, R. J., & Kneib, J. -P. 1999, *MNRAS*, 302, 632
- Bushouse, H. A. et al., 2002, *ApJS*, 138, 1
- Charmandaris, V., et al. 2002, *A&A*, 391, 429
- de Grijp, M. H. K., Miley, G. K., & Lub, J. 1987, *A&AS*, 70, 95
- Downes, D., & Solomon, P. M. 1998, *ApJ*, 507, 615
- Draine, B. T., & Lee, H. M. 1984, *ApJ*, 285, 89
- Dudley, C. C., & Wynn-Williams, C. G. 1997, *ApJ*, 488, 720
- Dudley, C. C., Imanishi, M., & Maloney, P. R. 2003, in *Astrophysics of Dust*, ed. A. N. Witt., G. C. Clayton, & B. T. Draine (San Francisco: ASP), p.191
- Fischer, J. 2000, in *ISO Beyond the Peaks*, ed. A. Salama, M. F. Kessler, K. Leech, & B. Schulz (ESA SP-456; Noordwijk: ESA), 239 (astro-ph/0009395)
- Forster Schreiber, N. M., Genzel, R., Lutz, D., Kunze, D., & Sternberg, A. 2001, *ApJ*, 552, 544
- Genzel, R. et al. 1998, *ApJ*, 498, 579
- Goldader, J. D., Joseph, R. D., Doyon, R., & Sanders, D. B. 1995, *ApJ*, 444, 97
- Imanishi, M. 2000, *MNRAS*, 319, 331
- Imanishi, M. 2002, *ApJ*, 569, 44
- Imanishi, M. 2003, *ApJ*, 599, 918
- Imanishi, M., & Alonso-Herrero, A. 2004, *ApJ*, 614, 122
- Imanishi, M., & Dudley, C. C. 2000, *ApJ*, 545, 701

- Imanishi, M., Dudley, C. C., & Maloney, P. R. 2001, *ApJ*, 558, L93
- Imanishi, M., & Maloney, P. R. 2003, *ApJ*, 588, 165
- Imanishi, M., Nakanishi, K., Kuno, N., & Kohno, K., 2004, *AJ*, 128, 2037
- Imanishi, M., Sasaki, Y., Goto, M., Kobayashi, N., Nagata, T., & Jones, T. J. 1996, *AJ*, 112, 235
- Imanishi, M., Terada, H., Goto, M., & Maihara, T. 1998, *PASJ*, 50, 399
- Imanishi, M., & Terashima, Y., 2004, *AJ*, 127, 758
- Imanishi, M., Terashima, Y., Anabuki, N., & Nakagawa, T. 2003, *ApJ*, 596, L167
- Imanishi, M., & Wada, K., 2004, *ApJ*, 617, 214
- Iye, M. et al., 2004, *PASJ*, 56, 381
- Keel, W. C., Irby, B. K., May, A., Miley, G. K., Golombek, D., de Grijp, M. H. K., & Gallimore, J. F. 2005, *ApJS*, 158, 139
- Kim, D. -C., & Sanders, D. B., 1998, *ApJS*, 119, 41
- Kim, D. -C., Veilleux, S., & Sanders, D. B., 2002, *ApJS*, 143, 277
- Kobayashi, N., et al. 2000, IRCS: Infrared camera and spectrograph for the Subaru Telescope, in *Proc. SPIE 4008: Optical and IR Telescope Instrumentation and Detectors*, eds M. Iye & A. F. Moorwood, 1056
- Lutz, D., Veilleux, S., & Genzel, R. 1999, *ApJ*, 517, L13
- Lutz, D. et al. 1996, *A&A*, 315, L269
- Maiolino, R. et al. 2003, *MNRAS*, 344, L59
- Maloney, P. R. 1999, *ApSS*, 266, 207
- Maloney, P., Hollenbach, D., & Tielens, A. G. G. M. 1996, *ApJ*, 466, 561
- Mathis, J. S., & Whiffen, G. 1989, *ApJ*, 341, 808
- McLeod, K. K., Rieke, G. H., Rieke, M. J., & Kelly, D. M. 1993, *ApJ*, 412, 111
- Mennella, V., Munoz Caro, G. M., Ruiterkamp, R., Schutte, W. A., Greenberg, J. M., Brucato, J. R., & Colangeli, L. 2001, *A&A*, 367, 355

- Moorwood, A. F. M. 1986, *A&A*, 166, 4
- Mountain, C. M., Robertson, D. J., Lee, T. J., & Wade, R. 1990, *Proc. SPIE*, 1235, 25
- Mouri, H., Kawara, K., Taniguchi, Y., & Nishida, M. 1990, *ApJ*, 356, L39
- Murakawa, K., Tamura, M., & Nagata, T. 2000, *ApJS*, 128, 603
- Murphy, Jr, T. W., Armus, L., Matthews, K., Soifer, B. T., Mazzarella, J. M., Shupe, D. L., Strauss, M. A., & Neugebauer, G. 1996, *AJ*, 111, 1025
- Murphy, T. W., Soifer, B. T., Matthews, K., Kiger, J. R., & Armus, L. 1999, *ApJ*, 525, L85
- Murphy, Jr, T. W., Soifer, B. T., Matthews, K., Armus, L., & Kiger, J. R. 2001, *AJ*, 121, 97
- Nagar, N. M., Wilson, A. S., Falcke, H., Veilleux, S., & Maiolino, R. 2003, *A&A*, 409, 115
- Neugebauer, G., Green, R. F., Matthews, K., Schmidt, M., Soifer, B. T., & Bennett, J. 1987, *ApJS*, 63, 615
- Normand, P., Rouan, D., Lacombe, F., & Tiphene, D. 1995, *A&A*, 297, 311
- Pendleton, Y. J., Sandford, S. A., Allamandola, L. J., Tielens, A. G. G. M., & Sellgren, K. 1994, *ApJ*, 437, 683
- Puxley, P. J. 1991, *MNRAS*, 249, 11p
- Rawlings, M. G., Adamson, A. J., & Whittet, D. C. B. 2003, *MNRAS*, 341, 1121
- Rayner, J. T., Toomey, D. W., Onaka, P. M., Denault, A. J., Stahlberger, W. E., Vacca, W. D., Cushing, M. C., & Wang, S. 2003, *PASP*, 115, 362
- Rhee, J. H., & Larkin, J. E. 2000, *ApJ*, 538, 98
- Rieke, G. H., & Lebofsky, M. J. 1985, *ApJ*, 288, 618
- Risaliti, G., et al. 2003, *ApJ*, 595, L17
- Risaliti, G., et al. 2005, *MNRAS*, submitted
- Robson, I. 1996, *Active Galactic Nuclei* (New York: Wiley)
- Sanders, D. B., & Mirabel, I. F. 1996, *ARA&A*, 34, 749
- Sanders, D. B., Soifer, B. T., Elias, J. H., Neugebauer, G., & Matthews, K. 1988, *ApJ*, 328, L35

- Scoville, N. Z. et al. 2000, *AJ*, 119, 991
- Sellgren, K. 1981, *ApJ*, 245, 138
- Shure, M. A., Toomey, D. W., Rayner, J. T., Onaka, P., & Denault, A. J. 1994, *Proc. SPIE*, 2198, 614
- Siebenmorgen, R., Krugel, E., & Spoon, H. W. W. 2004, *A&A*, 414, 123
- Smith, R. G., Sellgren K., & Tokunaga, A. T. 1989, *ApJ*, 344, 413
- Smith, R. G., Sellgren, K., & Brooke, T. Y. 1993, *MNRAS*, 263, 749
- Soifer, B. T., Neugebauer, G., Matthews, K., Egami, E., & Weinberger, A. J. 2002, *AJ*, 124, 2980
- Soifer, B. T., Sanders, D. B., Madore, B. F., Neugebauer, G., Danielson, G. E., Elias, J. H., Lonsdale, C. J., & Rice, W. L. 1987, *ApJ*, 320, 238
- Soifer, B. T. et al. 2000, *AJ*, 119, 509
- Spoon, H. W. W., Keane, J. V., Tielens, A. G. G. M., Lutz, D., & Moorwood, A. F. M. 2001, *A&A*, 365, L353
- Spoon, H. W. W., Keane, J. V., Tielens, A. G. G. M., Lutz, D., Moorwood, A. F. M., & Laurent, O. 2002, *A&A*, 385, 1022
- Spoon, H. W. W., Koornneef, J., Moorwood, A. F. M., Lutz, D., & Tielens, A. G. G. M. 2000, *A&A*, 357, 898
- Spoon, H. W. W., Moorwood, A. F. M., Lutz, D., Tielens, A. G. G. M., Siebenmorgen, R., & Keane, J. V. 2004, *A&A*, 414, 873
- Tanaka, M., Sato, S., Nagata, T., & Yamamoto, T. 1990, *ApJ*, 352, 724
- Taniguchi, Y., Kawara, K., Murayama, T., & Sato, Y. 1994, *AJ*, 107, 1668
- Taniguchi, Y., Yoshino, A., Ohyama, Y., & Nishiura, S. 1999, *ApJ*, 514, 660
- Tokunaga, A. T. 2000, in *Allen's Astrophysical Quantities*, ed. A. N. Cox (4th ed; Berlin: Springer), 143
- Tokunaga A. T., Sellgren K., Smith R. G., Nagata T., Sakata A., Nakada Y., 1991, *ApJ*, 380, 452

- Trung, D.-V., Lo, K. Y., Kim, D.-C., Gao, Y., & Gruendl, R. A. 2001, *ApJ*, 556, 141
- Veilleux, S., Kim, D.-C., & Sanders, D. B. 1999a, *ApJ*, 522, 113
- Veilleux, S., & Osterbrock, D. E. 1987, *ApJS*, 63, 295
- Veilleux, S., Sanders, D. B., & Kim, D.-C. 1997, *ApJ*, 484, 92
- Veilleux, S., Sanders, D. B., & Kim, D.-C. 1999b, *ApJ*, 522, 139
- Voit, G. M. 1992, *MNRAS*, 258, 841
- Whittet, D. C. B., Bode, M. F., Longmore, A. J., Adamson, A. J., McFadzean, A. D., Aitken, D. K., & Roche, P. F. 1988, *MNRAS*, 233, 321
- Willner, S. P., Ward, M., Longmore, A., Lawrence, A., Fabbiano, G., & Elvis, M., 1984, *PASP*, 96, 143
- Wynn-Williams, C. G. 1984, in *Galactic and Extragalactic Infrared Spectroscopy*, ed. M. F. Kessler, and J. P. Phillips (D. Reidel Publishing Company), 133
- Zhou, S., Wynn-Williams, C. G., & Sanders, D. B. 1993, *ApJ*, 409, 149

Table 1. Observed ULIRGs and their far-infrared emission properties.

Object	Redshift	$f_{12}$ (Jy)	$f_{25}$ (Jy)	$f_{60}$ (Jy)	$f_{100}$ (Jy)	$\log L_{\text{IR}}$ $L_{\odot}$	$f_{25}/f_{60}$	Optical Class
(1)	(2)	(3)	(4)	(5)	(6)	(7)	(8)	(9)
IRAS 00188–0856	0.128	<0.12	0.37	2.59	3.40	12.3	0.14 (C)	LINER
IRAS 03250+1606	0.129	<0.10	<0.15	1.38	1.77	12.1	<0.11 (C)	LINER
IRAS 08572+3915	0.058	0.32	1.70	7.43	4.59	12.1	0.23 (W)	LINER
IRAS 09039+0503	0.125	0.07	0.12	1.48	2.06	12.1	0.08 (C)	LINER
IRAS 09116+0334	0.146	<0.09	<0.14	1.09	1.82	12.2	<0.13 (C)	LINER
IRAS 09539+0857	0.129	<0.15	<0.15	1.44	1.04	12.0	<0.10 (C)	LINER
IRAS 10378+1108	0.136	<0.11	0.24	2.28	1.82	12.3	0.11 (C)	LINER
IRAS 10485–1447	0.133	<0.11	0.25	1.73	1.66	12.2	0.14 (C)	LINER
IRAS 10494+4424	0.092	<0.12	0.16	3.53	5.41	12.2	0.05 (C)	LINER
IRAS 11095–0238	0.106	0.06	0.42	3.25	2.53	12.2	0.13 (C)	LINER
IRAS 12112+0305	0.073	0.12	0.51	8.50	9.98	12.3	0.06 (C)	LINER
IRAS 12127–1412	0.133	<0.13	0.24	1.54	1.13	12.2	0.16 (C)	LINER
IRAS 12359–0725	0.138	0.09	0.15	1.33	1.12	12.1	0.11 (C)	LINER
IRAS 14252–1550	0.149	<0.09	<0.23	1.15	1.86	12.3	<0.20 (C)	LINER
IRAS 14348–1447	0.083	0.07	0.49	6.87	7.07	12.3	0.07 (C)	LINER
IRAS 15327+2340 (Arp 220)	0.018	0.48	7.92	103.33	112.40	12.1	0.08 (C)	LINER
IRAS 16090–0139	0.134	0.09	0.26	3.61	4.87	12.5	0.07 (C)	LINER
IRAS 16468+5200	0.150	<0.06	0.10	1.01	1.04	12.1	0.10 (C)	LINER
IRAS 16487+5447	0.104	<0.07	0.20	2.88	3.07	12.2	0.07 (C)	LINER
IRAS 17028+5817	0.106	<0.06	0.10	2.43	3.91	12.1	0.04 (C)	LINER
IRAS 17044+6720	0.135	<0.07	0.36	1.28	0.98	12.1	0.28 (W)	LINER
IRAS 21329–2346	0.125	0.05	0.12	1.65	2.22	12.1	0.07 (C)	LINER
IRAS 23234+0946	0.128	<0.06	0.08	1.56	2.11	12.1	0.05 (C)	LINER
IRAS 23327+2913	0.107	<0.06	0.22	2.10	2.81	12.1	0.10 (C)	LINER
IRAS 10190+1322	0.077	<0.07	0.38	3.33	5.57	12.0	0.11 (C)	HII
IRAS 11387+4116	0.149	0.12	<0.14	1.02	1.51	12.2	<0.14 (C)	HII
IRAS 11506+1331	0.127	<0.10	0.19	2.58	3.32	12.3	0.07 (C)	HII
IRAS 13443+0802	0.135	<0.12	<0.11	1.50	1.99	12.2	<0.07 (C)	HII <sup>a</sup>
IRAS 13509+0442	0.136	0.10	<0.23	1.56	2.53	12.3	<0.15 (C)	HII
IRAS 13539+2920	0.108	<0.09	0.12	1.83	2.73	12.1	0.07 (C)	HII
IRAS 14060+2919	0.117	<0.10	0.14	1.61	2.42	12.1	0.09 (C)	HII
IRAS 15206+3342	0.125	0.08	0.35	1.77	1.89	12.2	0.19 (C)	HII
IRAS 15225+2350	0.139	<0.07	0.18	1.30	1.48	12.2	0.14 (C)	HII
IRAS 16474+3430	0.111	<0.13	0.20	2.27	2.88	12.2	0.09 (C)	HII
IRAS 20414–1651	0.086	<0.65	0.35	4.36	5.25	12.3	0.08 (C)	HII
IRAS 21208–0519	0.130	<0.09	<0.15	1.17	1.66	12.1	<0.13 (C)	HII
IRAS 14197+0813	0.131	<0.17	<0.19	1.10	1.66	12.2	<0.17 (C)	unclassified
IRAS 14485–2434	0.148	<0.11	<0.15	1.02	1.05	12.2	<0.15 (C)	unclassified
IRAS 05189–2524	0.042	0.73	3.44	13.67	11.36	12.1	0.25 (W)	Sy2
IRAS 08559+1053	0.148	<0.10	0.19	1.12	1.95	12.2	0.17 (C)	Sy2
IRAS 12072–0444	0.129	<0.12	0.54	2.46	2.47	12.4	0.22 (W)	Sy2
IRAS 13428+5608 (Mrk 273)	0.037	0.24	2.28	21.74	21.38	12.1	0.10 (C)	Sy2
IRAS 13451+1232 (PKS 1345+12)	0.122	0.14	0.67	1.92	2.06	12.3	0.35 (W)	Sy2
IRAS 15130–1958	0.109	<0.14	0.39	1.92	2.30	12.1	0.20 (W)	Sy2



Table 1—Continued

Object	Redshift	$f_{12}$ (Jy)	$f_{25}$ (Jy)	$f_{60}$ (Jy)	$f_{100}$ (Jy)	$\log L_{\text{IR}}$ $L_{\odot}$	$f_{25}/f_{60}$	Optical Class
(1)	(2)	(3)	(4)	(5)	(6)	(7)	(8)	(9)
IRAS 17179+5444	0.147	<0.08	0.20	1.36	1.91	12.3	0.15 (C)	Sy2
IRAS 01572+0009 (Mrk 1014)	0.163	0.12	0.54	2.22	2.16	12.6	0.24 (W)	Sy1
IRAS 07599+6508	0.149	0.26	0.53	1.69	1.73	12.5	0.31 (W)	Sy1
IRAS 11598–0112	0.151	<0.14	<0.38	2.39	2.63	12.5	<0.16 (C)	Sy1
IRAS 12265+0219 (3C 273)	0.159	0.55	0.90	2.06	2.89	12.8	0.44 (W)	Sy1
IRAS 12540+5708 (Mrk 231)	0.042	1.87	8.66	31.99	30.29	12.5	0.27 (W)	Sy1
IRAS 15462–0450	0.100	0.10	0.45	2.92	3.00	12.2	0.15 (C)	Sy1
IRAS 21219–1757	0.112	0.21	0.45	1.07	1.18	12.1	0.42 (W)	Sy1

<sup>a</sup>The north-eastern nucleus (Kim et al. 2002) classified optically as an HII-region (Veilleux et al. 1999a) is observed.

Note. — Col.(1): Object name. Col.(2): Redshift. Col.(3)–(6):  $f_{12}$ ,  $f_{25}$ ,  $f_{60}$ , and  $f_{100}$  are *IRAS* fluxes at 12  $\mu\text{m}$ , 25  $\mu\text{m}$ , 60  $\mu\text{m}$ , and 100  $\mu\text{m}$ , respectively, taken from Kim & Sanders (1998). Col.(7): Decimal logarithm of infrared (8–1000  $\mu\text{m}$ ) luminosity in units of solar luminosity ( $L_{\odot}$ ), calculated with  $L_{\text{IR}} = 2.1 \times 10^{39} \times D(\text{Mpc})^2 \times (13.48 \times f_{12} + 5.16 \times f_{25} + 2.58 \times f_{60} + f_{100}) \text{ ergs s}^{-1}$  (Sanders & Mirabel 1996). Since the calculation is based on our adopted cosmology, the infrared luminosities slightly (<10%) differ from the values shown in Kim & Sanders (1998, their Table 1, column 15). For sources that have upper limits in some *IRAS* bands, we assume that the actual flux is the upper limit. Even though zero values are adopted, the difference of the infrared luminosities is very small, less than 0.2 dex, which will not affect our main conclusions in this paper. Col.(8): ULIRGs with  $f_{25}/f_{60} < 0.2$  and  $> 0.2$  are classified as cool and warm (denoted as “C” and “W”), respectively (Sanders et al. 1988). Col.(9): Optical spectral classification by Veilleux et al. (1999a).

Table 2. Observing log

Object	Date	Telescope	Integration	P.A. <sup>a</sup>	Name	Standard Stars	$T_{\text{eff}}$ (K)	
(1)	(UT)	Instrument	(Min)	( $^{\circ}$ )	(6)	$L$ -mag	Type	(9)
	(2)	(3)	(4)	(5)	(6)	(7)	(8)	(9)
IRAS 00188–0856	2002 August 19	Subaru IRCS	25	90	HR 72	5.0	G0V	5930
IRAS 03250+1606	2002 August 19	Subaru IRCS	23	0	HR 763	4.3	F7V	6240
IRAS 08572+3915 NW <sup>b</sup>	2003 March 18	IRTF SpeX	30	0	HR 3451	5.0	F7V	6240
IRAS 09039+0503	2005 February 21	Subaru IRCS	48	0	HR 3492	4.4	A0V	9480
IRAS 09116+0334 W	2005 February 20	Subaru IRCS	40	0	HR 3651	6.1	A0V	9480
IRAS 09539+0857	2005 February 22	Subaru IRCS	64	0	HR 3651	6.1	A0V	9480
IRAS 10378+1108	2005 February 21	Subaru IRCS	32	0	HR 4079	5.3	F6V	6400
IRAS 10485–1447	2005 February 21	Subaru IRCS	32	0	HR 4158	4.3	F7V	6240
IRAS 10494+4424	2005 February 20	Subaru IRCS	32	0	HR 4098	5.0	F9V	6000
IRAS 11095–0238	2005 February 21	Subaru IRCS	32	40 <sup>c</sup>	HR 4356	5.4	A0V	9480
IRAS 12112+0305 NE, SW	2004 February 8	Subaru IRCS	32	38 <sup>d</sup>	HR 4533	4.8	F7V	6240
IRAS 12127–1412 NE	2005 February 21	Subaru IRCS	16	0 <sup>e</sup>	HR 4529	4.9	F7V	6240
IRAS 12359–0725 N	2005 February 23	Subaru IRCS	40	0 <sup>f</sup>	HR 4533	4.8	F7V	6240
IRAS 14252–1550 E, W	2005 February 22	Subaru IRCS	80	125 <sup>g</sup>	HR 5355	5.9	A0	9480
IRAS 14348–1447 NE, SW	2005 May 28	Subaru IRCS	32	30 <sup>h</sup>	HR 5652	4.5	A0V	9480
IRAS 15327+2340 (Arp 220) <sup>i</sup>	2000 February 20	UKIRT CGS4	64	90	HR 5634	3.8	F5V	6500
IRAS 16090–0139	2003 May 18	Subaru IRCS	14	0	HR 5859	5.6	A0V	9480
IRAS 16468+5200 E	2005 February 23	Subaru IRCS	72	85 <sup>j</sup>	HR 5949	6.3	A0V	9480
IRAS 16487+5447 W	2002 March 28	Subaru IRCS	36	70 <sup>k</sup>	HR 5949	6.3	A0V	9480
IRAS 17028+5817 W	2004 June 12	Subaru IRCS	20	175 <sup>l</sup>	HR 5949	6.3	A0V	9480
IRAS 17044+6720	2005 June 13	Subaru IRCS	26	90	HR 6025	5.4	A0V	9480
IRAS 21329–2346	2002 October 24	Subaru IRCS	32	90	HR 7898	4.5	G8V	5400
IRAS 23234+0946 W	2002 October 24	Subaru IRCS	32	120 <sup>m</sup>	HR 8653	4.6	G8IV	5400
IRAS 23327+2913 S	2002 October 24	Subaru IRCS	24	90 <sup>n</sup>	HR 8955	5.1	F6V	6400
IRAS 10190+1322 E,W	2005 February 22	Subaru IRCS	32	65 <sup>o</sup>	HR 3998	5.1	F7V	6240
IRAS 11387+4116	2005 February 23	Subaru IRCS	32	0	HR 4345	5.0	G0V	5930
IRAS 11506+1331	2005 February 22	Subaru IRCS	32	0	HR 4437	4.7	G0V	5930
IRAS 13443+0802 NE	2005 May 28	Subaru IRCS	24	170 <sup>p</sup>	HR 5243	4.9	F6V	6400
IRAS 13509+0442	2005 February 22	Subaru IRCS	32	0	HR 5011	3.8	G0V	5930
IRAS 13539+2920 NW	2004 June 12	Subaru IRCS	20	0 <sup>q</sup>	HR 5346	4.8	F8V	6000
IRAS 14060+2919	2005 June 12	Subaru IRCS	18	0	HR 5346	4.8	F8V	6000
IRAS 15206+3342	2005 June 13	Subaru IRCS	18	0	HR 5728	4.5	G3V	5800
IRAS 15225+2350	2005 February 20	Subaru IRCS	32	0	HR 5630	5.0	F8V	6000

Table 2—Continued

Object	Date	Telescope	Integration	P.A. <sup>a</sup>	Name	Standard Stars		
(1)	(UT)	Instrument	(Min)	( $^{\circ}$ )	(6)	<i>L</i> -mag	Type	$T_{\text{eff}}$ (K)
(1)	(2)	(3)	(4)	(5)	(6)	(7)	(8)	(9)
IRAS 16474+3430 S	2005 February 21	Subaru IRCS	32	161 <sup>r</sup>	HR 6064	5.2	G1V	5900
IRAS 20414–1651	2005 May 28	Subaru IRCS	24	0	HR 7855	4.9	F6V	6400
IRAS 21208–0519 N	2005 May 28	Subaru IRCS	20	17 <sup>s</sup>	HR 8041	4.7	G1V	5900
IRAS 14197+0813	2005 May 28	Subaru IRCS	32	0	HR 5307	5.1	F7V	6240
IRAS 14485–2434	2005 May 28	Subaru IRCS	24	0	HR 5504	5.0	F7V	6240
IRAS 05189–2524 <sup>i</sup>	1999 September 9	UKIRT CGS4	53	19	HR 1762	4.7	A0V	9480
IRAS 08559+1053	2005 February 23	Subaru IRCS	24	0	HR 3510	4.9	G1V	5900
IRAS 12072–0444 N, S	2005 May 29	Subaru IRCS	16	0 <sup>t</sup>	HR 4533	4.8	F7V	6240
IRAS 13428+5608 (Mrk 273) <sup>i</sup>	2000 February 20	UKIRT CGS4	43	35	HR 4761	4.8	F6-8V	6200
IRAS 13451+1232 W (PKS 1345+12)	2005 February 23	Subaru IRCS	32	105 <sup>u</sup>	HR 5011	3.8	G0V	5930
IRAS 15130–1958	2005 May 28	Subaru IRCS	12	0	HR 5504	5.0	F7V	6240
IRAS 17179+5444	2005 May 28	Subaru IRCS	16	0	HR 6360	4.5	G5V	5700
IRAS 01572+0009 (Mrk 1014)	2003 September 8	IRTF SpeX	160	0	HR 650	4.1	F8V	6000
IRAS 07599+6508	2004 April 4	IRTF NSFCAM	40	0	HR 3028	4.8	F6V	6400
IRAS 11598–0112	2005 May 29	Subaru IRCS	8	0	HR 4533	4.8	F7V	6240
IRAS 12265+0219 (3C 273)	2004 April 5	IRTF NSFCAM	28	0	HR 4708	5.0	F8V	6000
IRAS 12540+5708 (Mrk 231) <sup>v</sup>	2000 February 20	UKIRT CGS4	21	0	HR 4761	4.8	F6-8V	6200
IRAS 15462–0450	2004 April 5	IRTF NSFCAM	120	0	HR 5779	5.2	F7V	6240
IRAS 21219–1757	2005 May 29	Subaru IRCS	8	0	HR 7994	4.9	G1V	5900

Note. — Column (1): Object name. Col. (2): Observing date in UT. Col. (3): Telescope and instrument. Col. (4): Net on-source integration time in min. Col. (5): Position angle of the slit. Col. (6): Standard star name. Col. (7): Adopted *L*-band magnitude. Col. (8): Stellar spectral type. Col. (9): Effective temperature.

<sup>a</sup>0 $^{\circ}$  corresponds to the north-south direction. Position angle increases with counter-clockwise on the sky plane.

<sup>b</sup>A spectrum at  $\lambda = 3.2\text{--}3.8 \mu\text{m}$  was shown by Imanishi & Dudley (2000). We present a new spectrum with a wider wavelength coverage of  $\lambda = 2.8\text{--}4.1 \mu\text{m}$ , to investigate a broad  $3.1 \mu\text{m}$  H<sub>2</sub>O ice absorption feature. We observed the north-western nucleus which is much brighter in the infrared *L*-band than the south-eastern nucleus (Zhou et al. 1993).

<sup>c</sup>To simultaneously observe double nuclei with a separation of  $\sim 0''.5$  (Bushouse et al. 2002). In our spectrum, a double peak along the slit direction is recognizable, but signals from the double nuclei are not clearly resolvable. A spectrum combining both nuclei is presented in this paper.

<sup>d</sup>To simultaneously observe double nuclei with a separation of  $\sim 3''$  (Scoville et al. 2000; Kim et al. 2002).

<sup>e</sup>Only the brighter north-eastern nucleus (Kim et al. 2002) was observed.

<sup>f</sup>Only the northern primary nucleus (Trung et al. 2001) was observed.

<sup>g</sup>The south-western nucleus (Kim et al. 2002) was resolved into double nuclei (eastern and western) with a separation of  $\sim 1''.1$  in our *K*-band image. Both the eastern and western nuclei were observed.

<sup>h</sup>To simultaneously observe double nuclei with a separation of  $\sim 3''$  (Scoville et al. 2000; Kim et al. 2002; Charmandaris et al. 2002).

<sup>i</sup>The same spectrum as previously shown by Imanishi & Dudley (2000) is presented again. The wavelength coverage is narrower than the other ULIRGs.

<sup>j</sup>To simultaneously observe double nuclei with a separation of  $\sim 3''.5$  (Kim et al. 2002). Only the eastern nucleus was bright enough to extract a meaningful *L*-band spectrum.

<sup>k</sup>To simultaneously observe double nuclei with a separation of  $\sim 3''$  (Murphy et al. 1996; Kim et al. 2002). Only the western primary nucleus (Murphy et al. 2001) was bright enough to extract a meaningful *L*-band spectrum.

<sup>l</sup>Only the western primary nucleus (Trung et al. 2001) was observed.

<sup>m</sup>To simultaneously observe double nuclei with a separation of  $\sim 4''$  in the *K*-band image (Kim et al. 2002). Only the western nucleus was bright enough to extract a meaningful *L*-band spectrum.

<sup>n</sup>Only the southern primary nucleus (Trung et al. 2001) was observed.

<sup>o</sup>To simultaneously observe double nuclei with a separation of  $\sim 4''$  (Kim et al. 2002).

<sup>p</sup>To simultaneously observe north-eastern and eastern nuclei with a separation of  $\sim 5''$  (Kim et al. 2002). Both nuclei were detected, but only the north-eastern nucleus was bright enough to extract a meaningful *L*-band spectrum.

<sup>q</sup>Only the north-western primary nucleus (Kim et al. 2002) was observed.

<sup>r</sup>To simultaneously observe double nuclei with a separation of  $\sim 3''.5$  (Kim et al. 2002). Only the southern nucleus was bright enough to extract a meaningful *L*-band spectrum.

<sup>s</sup>To simultaneously observe double nuclei with a separation of  $\sim 7''$  (Kim et al. 2002). Only the northern nucleus was bright enough to extract a meaningful *L*-band spectrum.

<sup>t</sup>The nucleus (Kim et al. 2002) was resolved into double nuclei (northern and southern) with a separation of  $\sim 0''.9$  in our *K*-band image. Both nuclei were observed.

<sup>u</sup>To simultaneously observe double nuclei with a separation of  $\sim 2''$  (Scoville et al. 2000). Only the western AGN-harboring main nucleus (Imanishi & Terashima 2004) was bright enough to extract a meaningful *L*-band spectrum.

<sup>v</sup>*L*-band spectra have previously been presented by Imanishi et al. (1998) and Imanishi & Dudley (2000). The spectrum by Imanishi & Dudley (2000) is shown again. The wavelength coverage is narrower than the other ULIRGs.

Table 3. Properties of the nuclear 3.3  $\mu\text{m}$  PAH emission and buried AGN signatures.

Object	$f_{3.3\text{PAH}}$ ( $\times 10^{-14}$ ergs s $^{-1}$ cm $^{-2}$ )	$L_{3.3\text{PAH}}$ ( $\times 10^{41}$ ergs s $^{-1}$ )	$L_{3.3\text{PAH}}/L_{\text{IR}}$ ( $\times 10^{-3}$ )	rest EW $_{3.3\text{PAH}}$ (nm)	AGN evidence	
(1)	(2)	(3)	(4)	(5)	L-band (6)	Radio (7)
IRAS 00188–0856	3.5	13	0.15	50	○	○ (0.6)
IRAS 03250+1606	3.0	12	0.25	80	○	X
IRAS 08572+3915 NW	<3.5 <sup>a</sup>	<2.5 <sup>a</sup>	<0.05 <sup>a</sup>	<5 <sup>a</sup>	⊙	○ (0.8)
IRAS 09039+0503	1.5	5.5	0.10	95	○	X
IRAS 09116+0334 W	3.0	15	0.25	75	○	X
IRAS 09539+0857	0.9	3.5	0.07	65	X	○ (1.0)
IRAS 10378+1108	1.0	4.5	0.06	40	○	○ (0.8)
IRAS 10485–1447	2.0	7.0	0.10	80	○	—
IRAS 10494+4424	3.5	6.5	0.10	110	○	○ (0.4)
IRAS 11095–0238	2.5	6.0	0.10	150	X	—
IRAS 12112+0305 NE	3.5	4.0	0.05	100	X	○ (0.8)
IRAS 12112+0305 SW	3.5	4.0	0.05	160	X	X
IRAS 12127–1412 NE	0 <sup>b</sup>	0 <sup>b</sup>	0 <sup>b</sup>	0 <sup>b</sup>	⊙	—
IRAS 12359–0725 N	2.0	9.5	0.20	75	○	—
IRAS 14252–1550 E	0.7	3.5	0.06	60	○	—
IRAS 14252–1550 W	0.7	3.5	0.06	60	X	—
IRAS 14348–1447 NE	1.5	2.0	0.03	70	○	—
IRAS 14348–1447 SW	3.5	5.0	0.07	110	X	—
IRAS 15327+2340 (Arp 220)	25	1.5	0.03	80	X	○ (0.2)
IRAS 16090–0139	3.0	13	0.10	75	○	—
IRAS 16468+5200 E	1.0	5.5	0.10	120	X	X
IRAS 16487+5447 W	2.5	6.0	0.10	70	○	○ (0.7)
IRAS 17028+5817 W	4.0	10	0.20	120	○	○ (0.9)
IRAS 17044+6720	2.0	8.5	0.15	10	⊙	○ (1.3)
IRAS 21329–2346	1.0	4.0	0.08	50	○	—
IRAS 23234+0946 W	2.5	10	0.20	75	X	○ (0.4)
IRAS 23327+2913 S	2.0	5.0	0.10	45	X	X
IRAS 10190+1322 E	5.5	7.0	0.20	95	X	○ (1.0)
IRAS 10190+1322 W	1.0	1.5	0.04	50	X	X
IRAS 11387+4116	1.5	8.0	0.15	75	X	X
IRAS 11506+1331	5.5	21	0.25	95	○	○ (0.3)
IRAS 13443+0802 NE	1.0	5.0	0.08	75	X	○ (0.7)
IRAS 13509+0442	4.0	18	0.25	135	X	X

Table 3—Continued

Object	$f_{3.3\text{PAH}}$ ( $\times 10^{-14}$ ergs s $^{-1}$ cm $^{-2}$ )	$L_{3.3\text{PAH}}$ ( $\times 10^{41}$ ergs s $^{-1}$ )	$L_{3.3\text{PAH}}/L_{\text{IR}}$ ( $\times 10^{-3}$ )	rest EW $_{3.3\text{PAH}}$ (nm)	AGN evidence L-band	Radio
(1)	(2)	(3)	(4)	(5)	(6)	(7)
IRAS 13539+2920 NW	4.5	11	0.25	85	X	○ (0.2)
IRAS 14060+2919	7.5	23	0.45	150	X	X
IRAS 15206+3342	4.0	14	0.25	55	X	X
IRAS 15225+2350	1.5	7.0	0.15	40	○	○ (1.0)
IRAS 16474+3430 S	5.0	14	0.25	105	○	X
IRAS 20414–1651	2.5	4.0	0.05	75	X	○ (0.7)
IRAS 21208–0519 N	1.5	6.0	0.10	100	X	X
IRAS 14197+0813	2.0	7.5	0.15	90	○	○ <sup>c</sup> (?)
IRAS 14485–2434	2.5	13.5	0.25	70	○	—
IRAS 05189–2524	11	4.0	0.09	4	⊙	—
IRAS 08559+1053	3.5	17	0.25	10	⊙	X
IRAS 12072–0444 S	1.0	3.5	0.04	45	⊙	—
IRAS 12072–0444 N	2.0	8.0	0.09	20	⊙	—
IRAS 13428+5608 (Mrk 273)	14	4.0	0.09	35	⊙	○ (0.4)
IRAS 13451+1232 W (PKS 1345+12)	<2.5	<7.0	<0.10	<5	⊙	○ (0.9)
IRAS 15130–1958	3.5	9.0	0.15	10	⊙	—
IRAS 17179+5444	1.0	6.0	0.09	20	⊙	○ (0.9)
IRAS 01572+0009 (Mrk 1014)	3.0	21	0.15	7	⊙	○ (1.0)
IRAS 07599+6508	<7.5	<40	<0.35	<4	⊙	○ (0.8)
IRAS 11598–0112	1.5	7.0	0.06	4	⊙	—
IRAS 12265+0219 (3C 273)	<7.0	<40	<0.20	<2	⊙	○ (1.0)
IRAS 12540+5708 (Mrk 231)	18	6.0	0.05	2	⊙	○ (0.9)
IRAS 15462–0450	3.5	7.0	0.15	10	⊙	—
IRAS 21219–1757	1.0	2.5	0.05	1	⊙	○ (1.0)

<sup>a</sup>A conservative upper limit of the 3.3  $\mu\text{m}$  PAH emission was estimated based on our new spectrum, and is larger than our original estimate (Imanishi & Dudley 2000).

<sup>b</sup>The upper limit of the 3.3  $\mu\text{m}$  PAH emission is difficult to estimate, because of the winding spectral shape. The observed profiles are explained by absorption features, and so we adopt the PAH flux as zero.

<sup>c</sup>We classify IRAS 14197+0813 as a ULIRG with detectable core emission, based on column 9 of Table 1 in Nagar et al. (2003).

Note. — Col. (1): Object name. Col. (2): Observed flux of the 3.3  $\mu\text{m}$  PAH emission. The second effective digit, if smaller than unity, is shown

in units of 0.5. Col. (3): Observed luminosity of the  $3.3 \mu\text{m}$  PAH emission. Col. (4): Observed  $3.3 \mu\text{m}$  PAH-to-infrared luminosity ratio in units of  $10^{-3}$ , a typical value for less infrared luminous starbursts (Mouri et al. 1990; Imanishi 2002). Col. (5): Rest-frame equivalent width of the  $3.3 \mu\text{m}$  PAH emission. Those for starbursts are  $\sim 100 \text{ nm}$  (Moorwood 1986; Imanishi & Dudley 2000). Col. (6): Evidence of an AGN from our  $L$ -band spectroscopic method.  $\odot$ : strong evidence.  $\circ$ : tentative evidence. X: no evidence. Col. (7): VLA radio data by Nagar et al. (2003).  $\odot$ : core detected. X: undetected. —: no data. The values in parentheses are the core-to-total radio flux ratio in mJy, taken from Nagar et al. (2003).

Table 4. Absorption features in the  $L$ -band

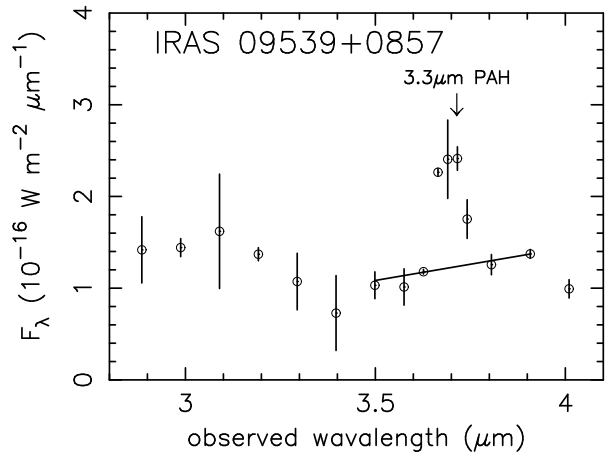
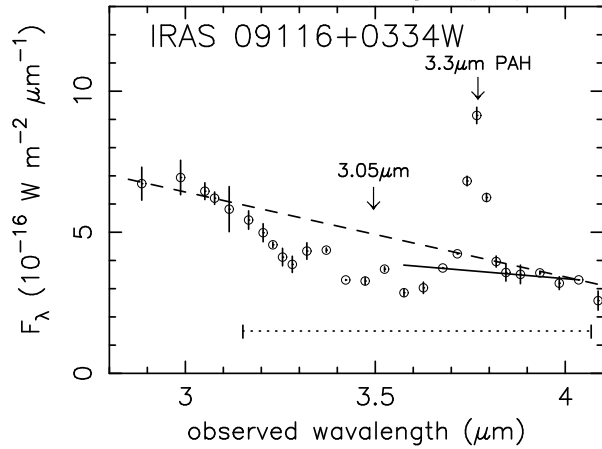
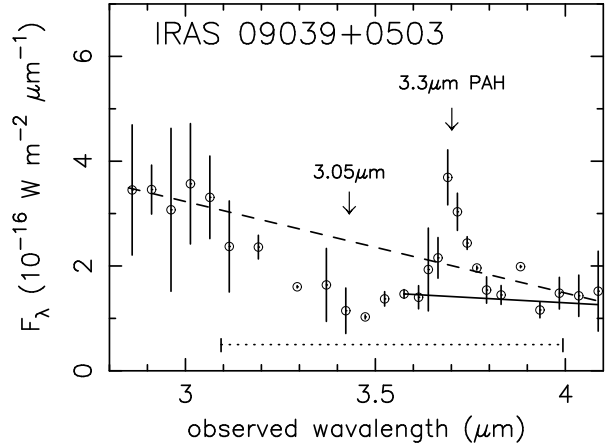
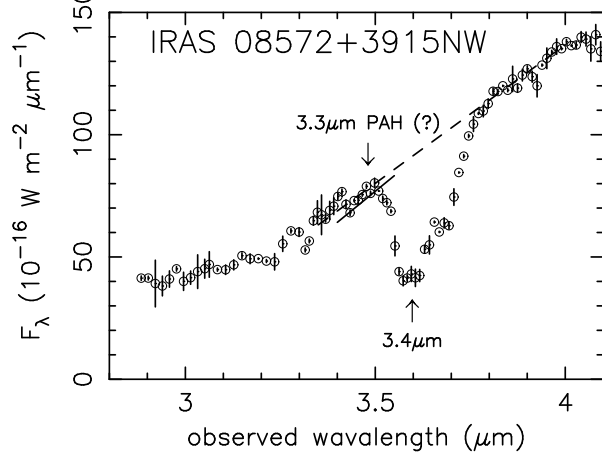
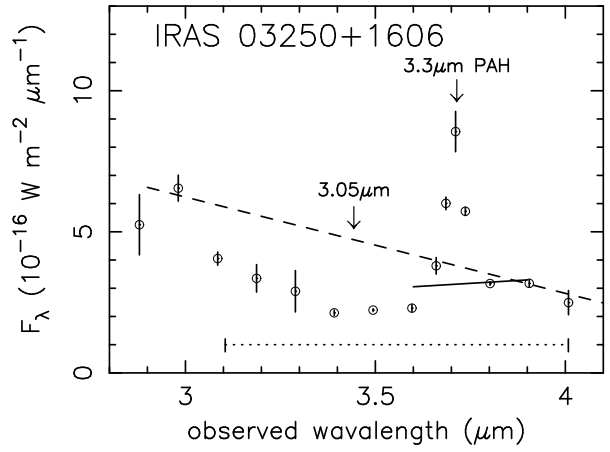
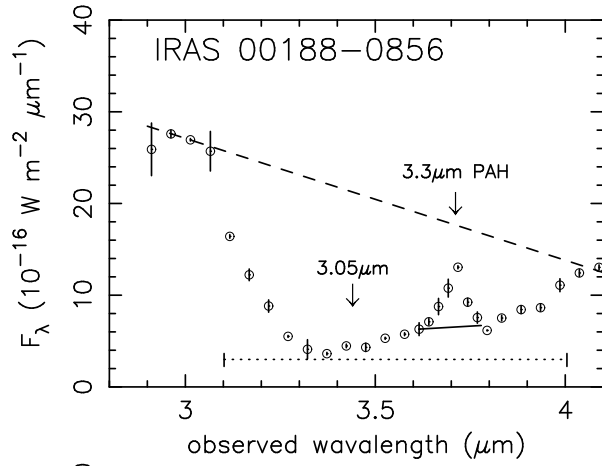
Object (1)	observed $\tau_{3.1}$ (2)	observed $\tau_{3.4}$ (3)	$A_V$ [mag] (4)
IRAS 00188–0856	1.8	...	>30
IRAS 03250+1606	0.8	...	>13
IRAS 08572+3915 NW	...	0.8	110–200
IRAS 09039+0503	0.8	...	>13
IRAS 09116+0334 W	0.4	...	>6
IRAS 10378+1108	0.6	...	>10
IRAS 10485+1108	0.8	...	>13
IRAS 10494+4424	1.0	...	>16
IRAS 12127–1412 NE	0.4	0.35	56–94
IRAS 12359–0725 N	0.5	...	>8
IRAS 14252–1550 E	0.7	...	>11
IRAS 14348–1447 NE	0.5	...	>8
IRAS 16090–0139	0.8	...	>13
IRAS 16487+5447 W	1.2	...	>20
IRAS 17028+5817 W	0.6	...	>10
IRAS 17044+6720	...	0.15	21–38
IRAS 21329–2346	1.0	...	>16
IRAS 11506+1331	1.0	...	>16
IRAS 15225+2350	0.4	...	>6
IRAS 16474+3430 S	0.8	...	>13
IRAS 14197+0813	0.4	...	>6
IRAS 14485–2434	0.4	...	>6
IRAS 12072–0444 N	...	0.4	57–100

Note. — Col. (1): Object name. Only ULIRGs which show clear absorption features are listed. LINER, HII, optically-unclassified, and Seyfert-2 ULIRGs (from the top to the bottom) are separated by the horizontal solid lines. Col. (2): Observed optical depth of the  $3.1 \mu\text{m}$

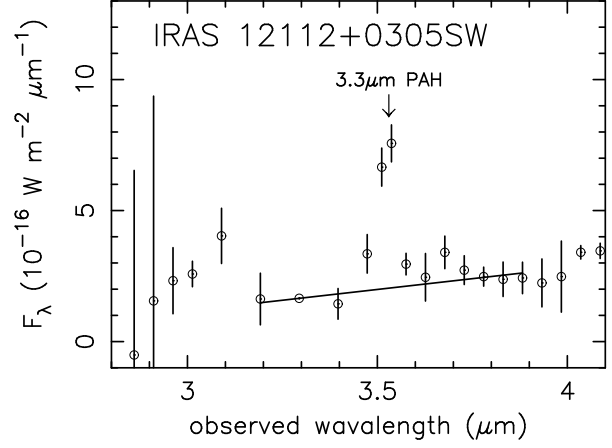
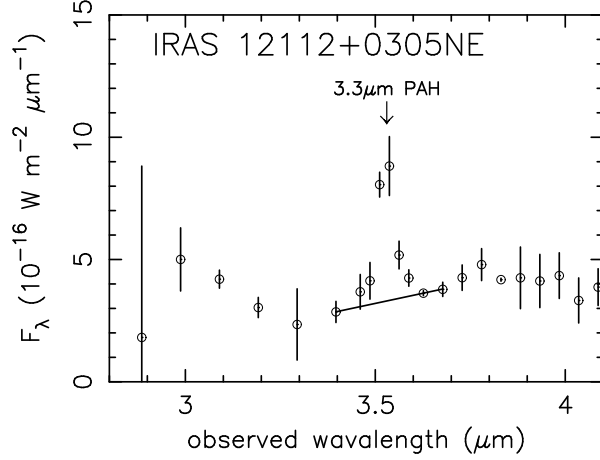
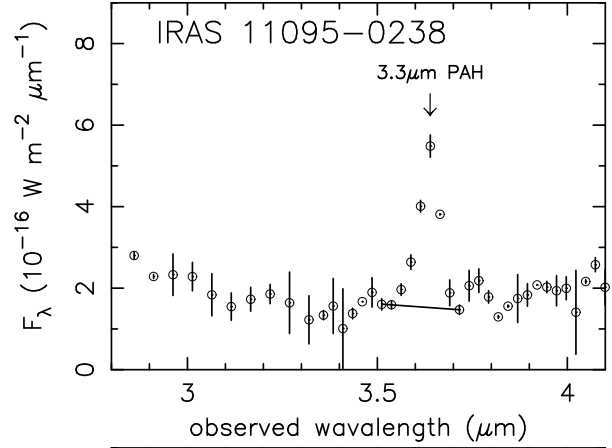
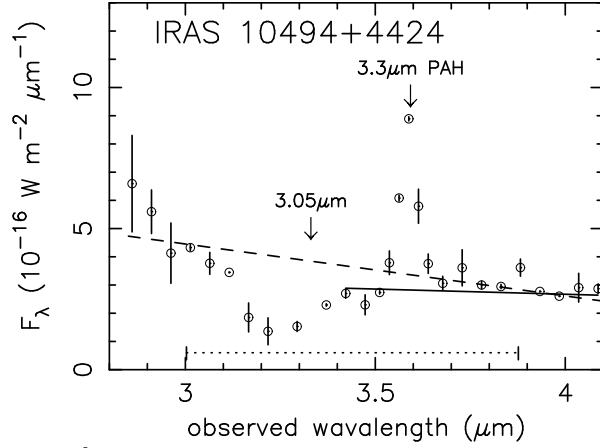
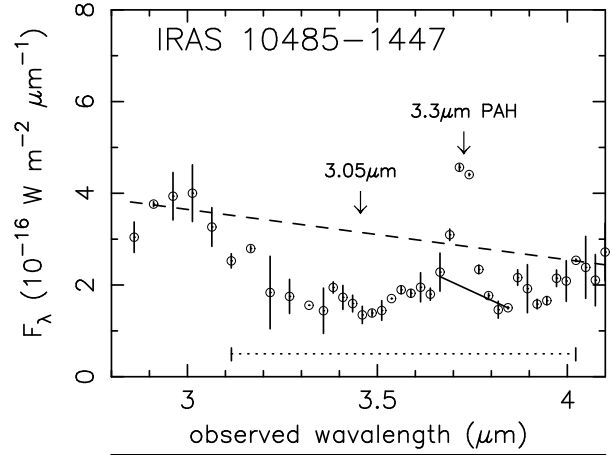
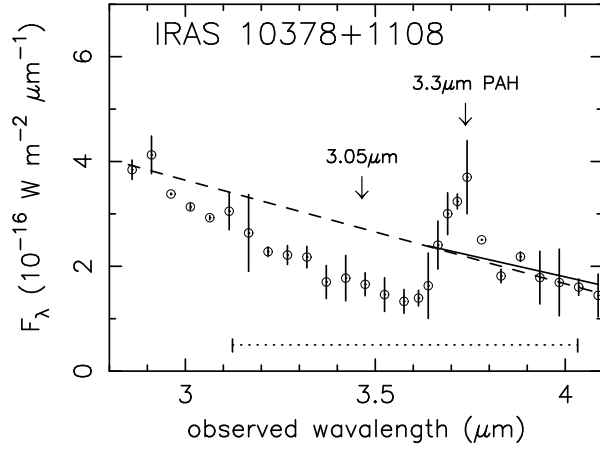


H<sub>2</sub>O ice absorption feature. Since relatively low plausible continuum levels are adopted, these values should be taken as conservative lower limits. The  $\tau_{3.1}$  values are derived by combining a few data points around the ice absorption peak, and the statistical errors are at a level of  $<0.1$ . Col. (3): Observed optical depth of the 3.4  $\mu\text{m}$  bare carbonaceous dust absorption feature. Col. (4): Dust extinction in  $A_V$  toward the 3–4  $\mu\text{m}$  continuum emission regions, derived from the absorption optical depths, assuming the Galactic dust extinction curve. For those with detected 3.1  $\mu\text{m}$  absorption, but with no measurable  $\tau_{3.4}$  values, the derived  $A_V$  values should be taken as lower limits (see text in §5.4).

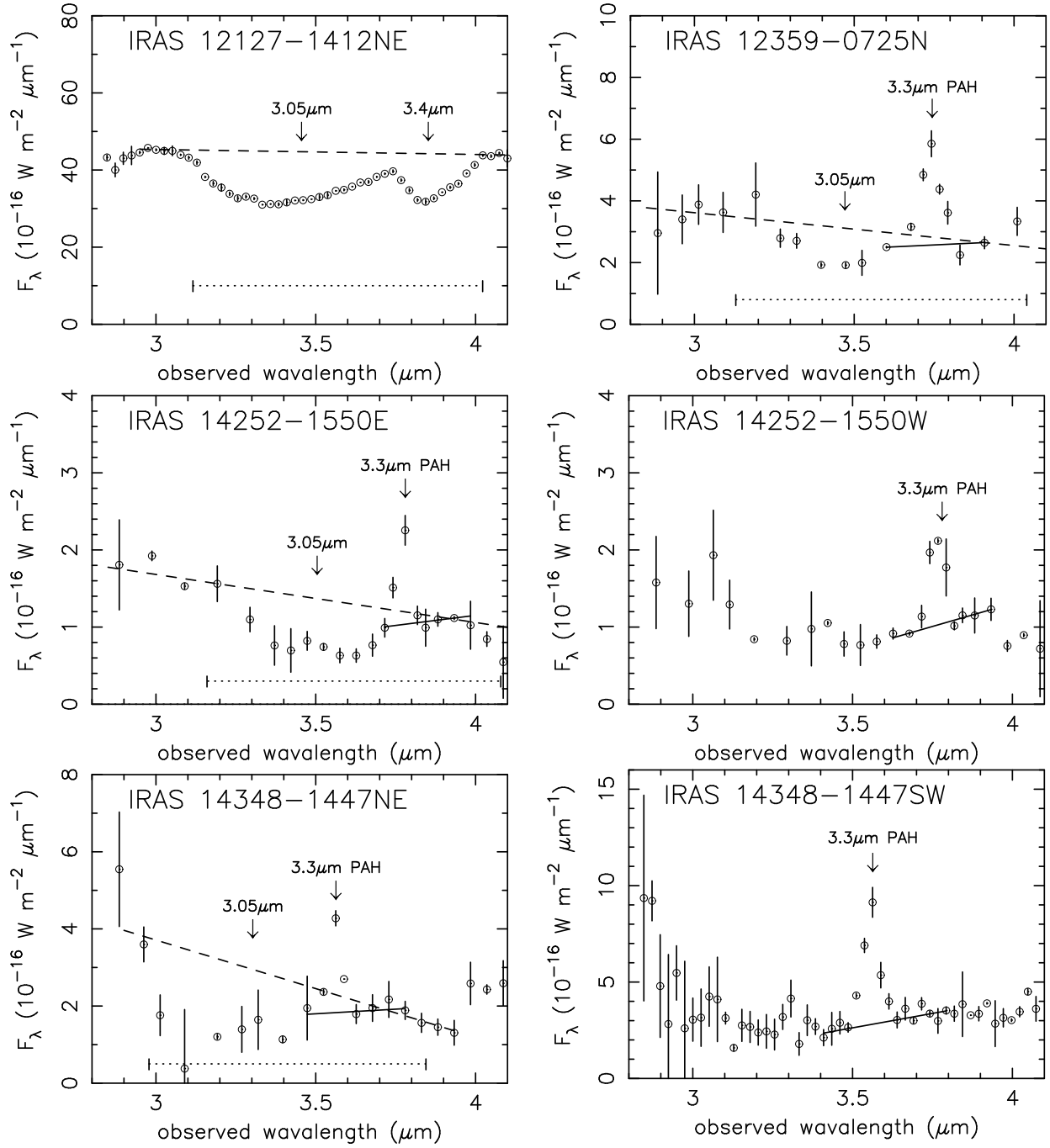
# LINER (1)



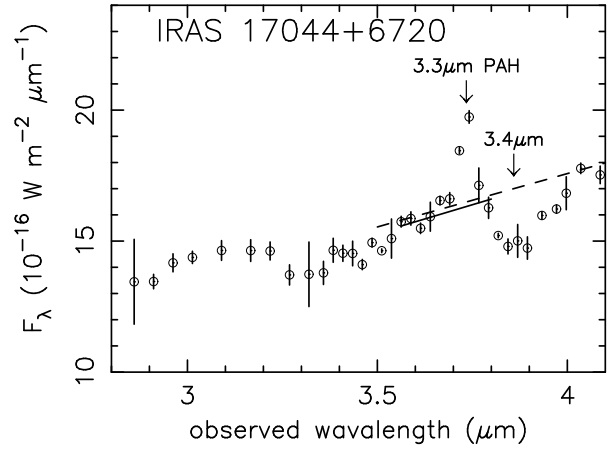
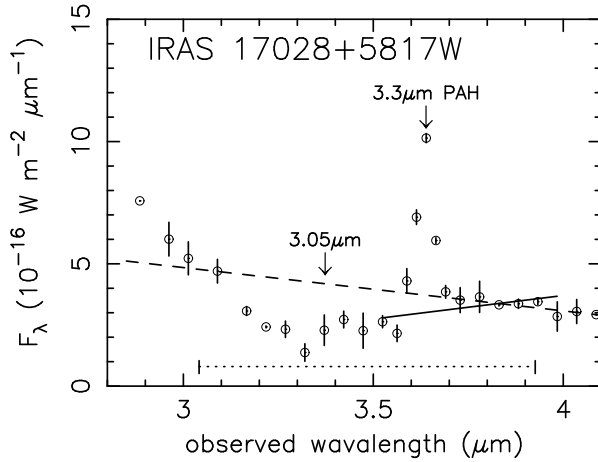
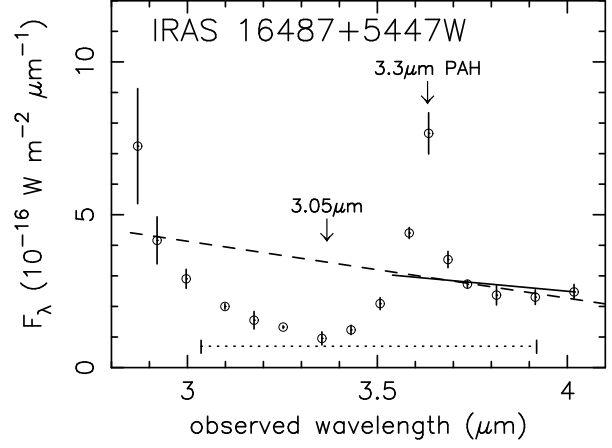
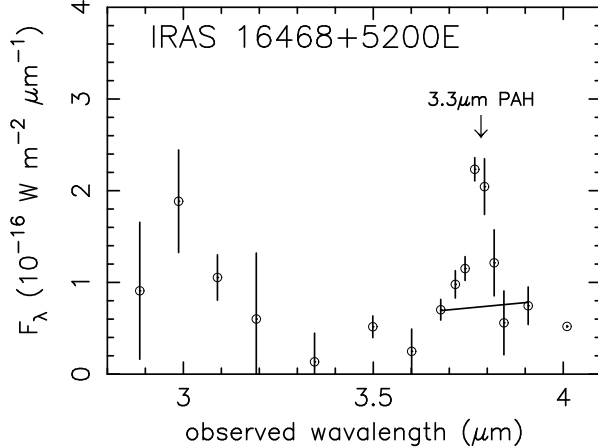
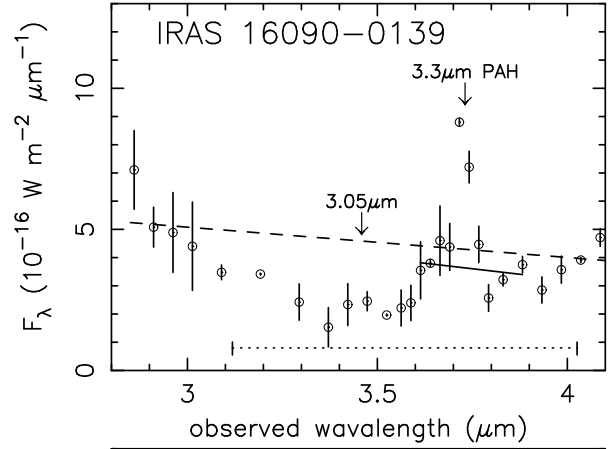
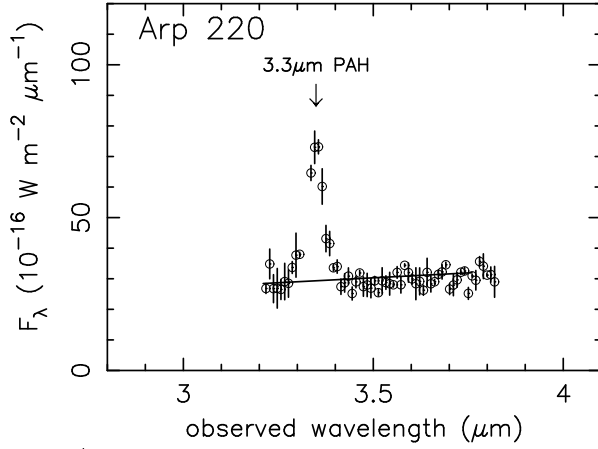
## LINER (2)



### LINER (3)



# LINER (4)



## LINER (5)

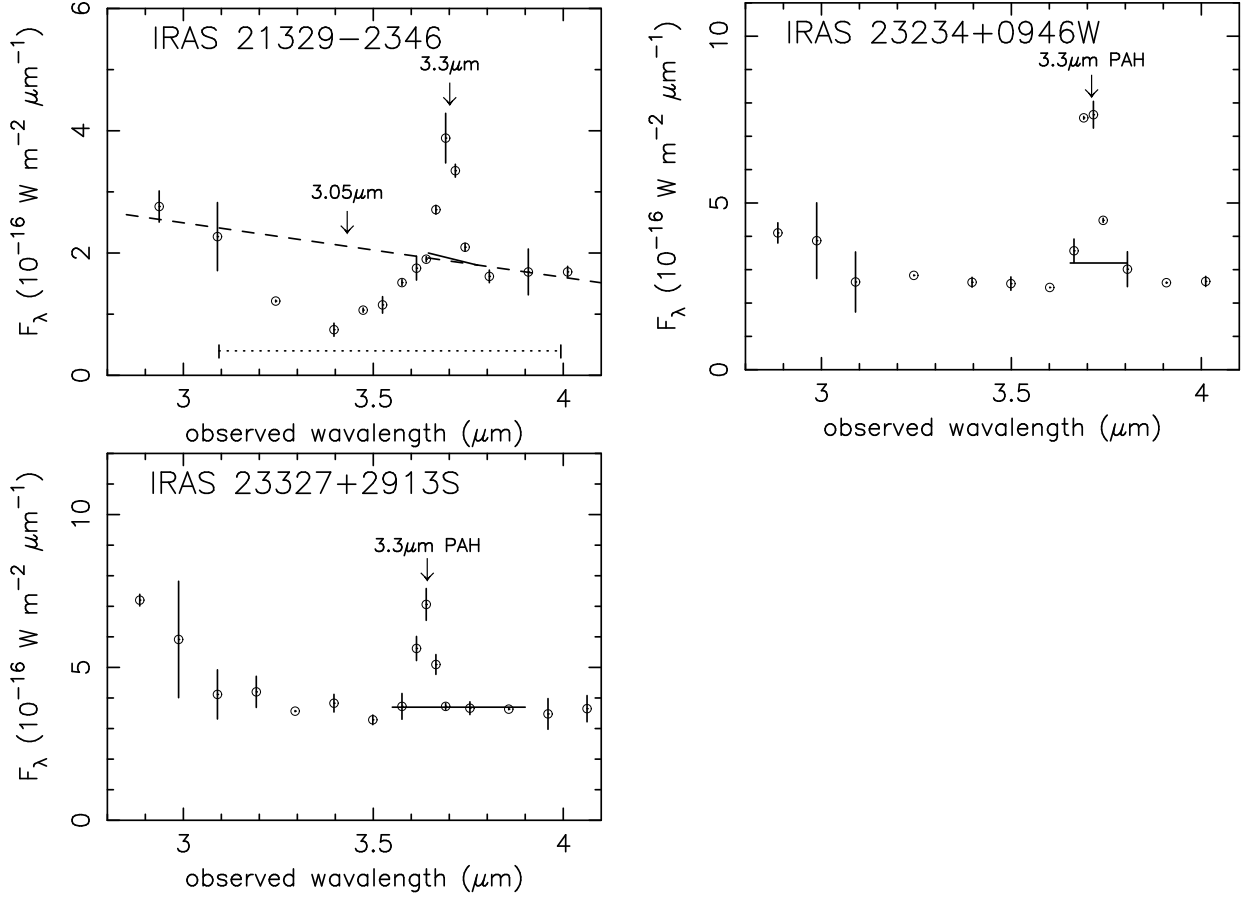
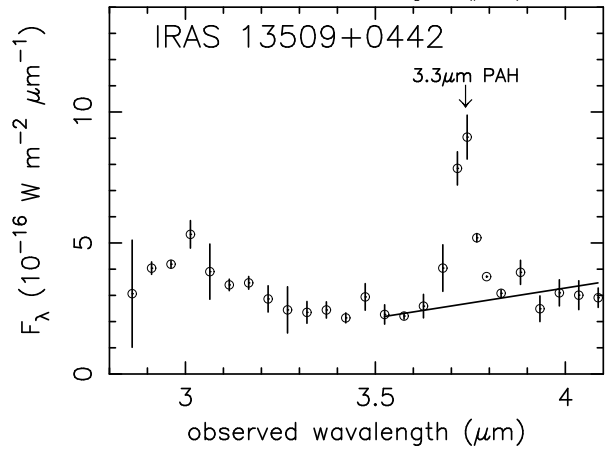
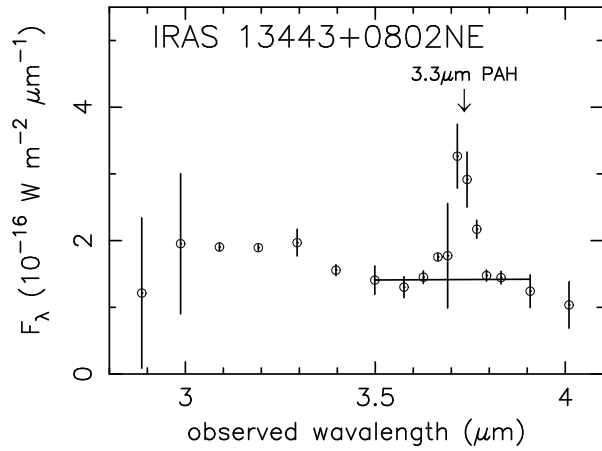
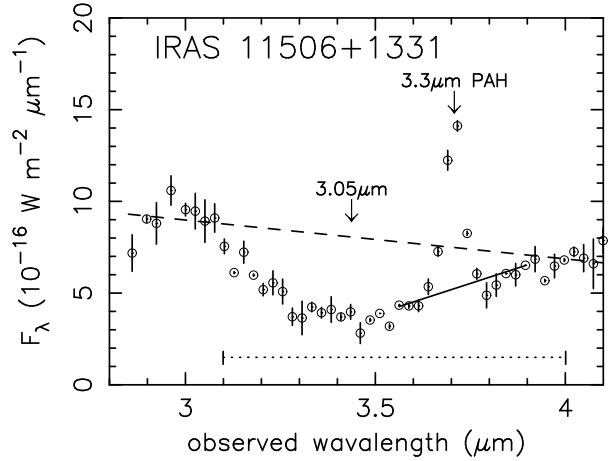
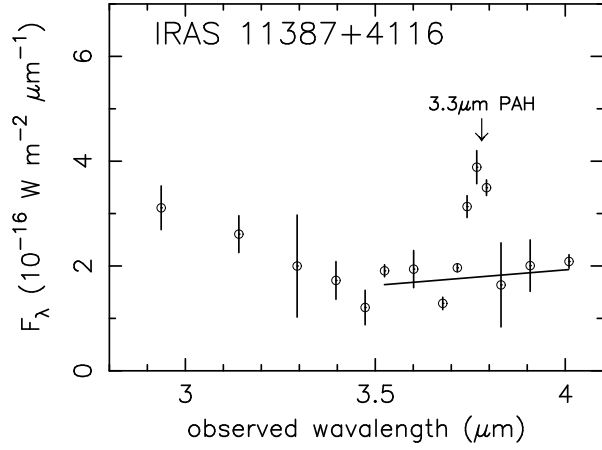
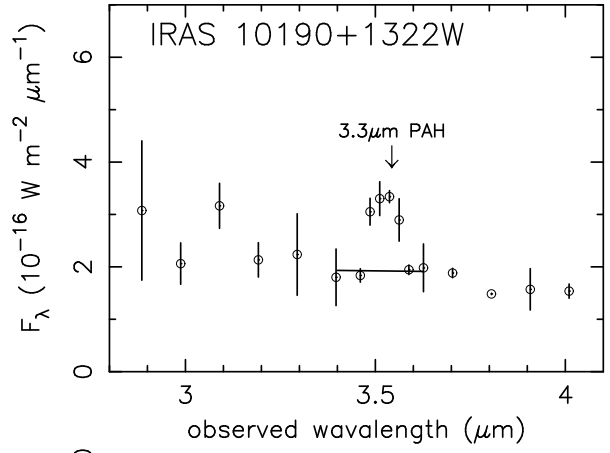
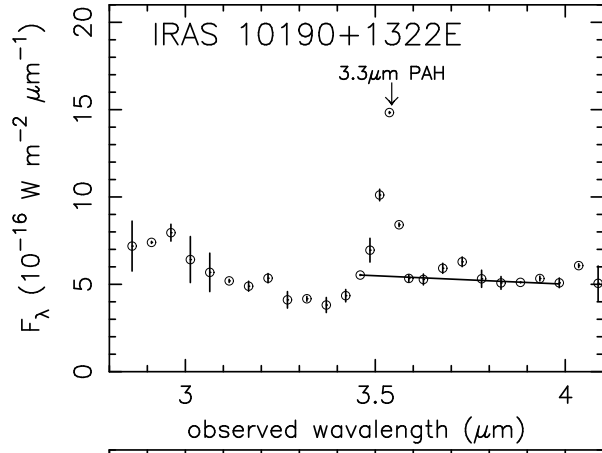
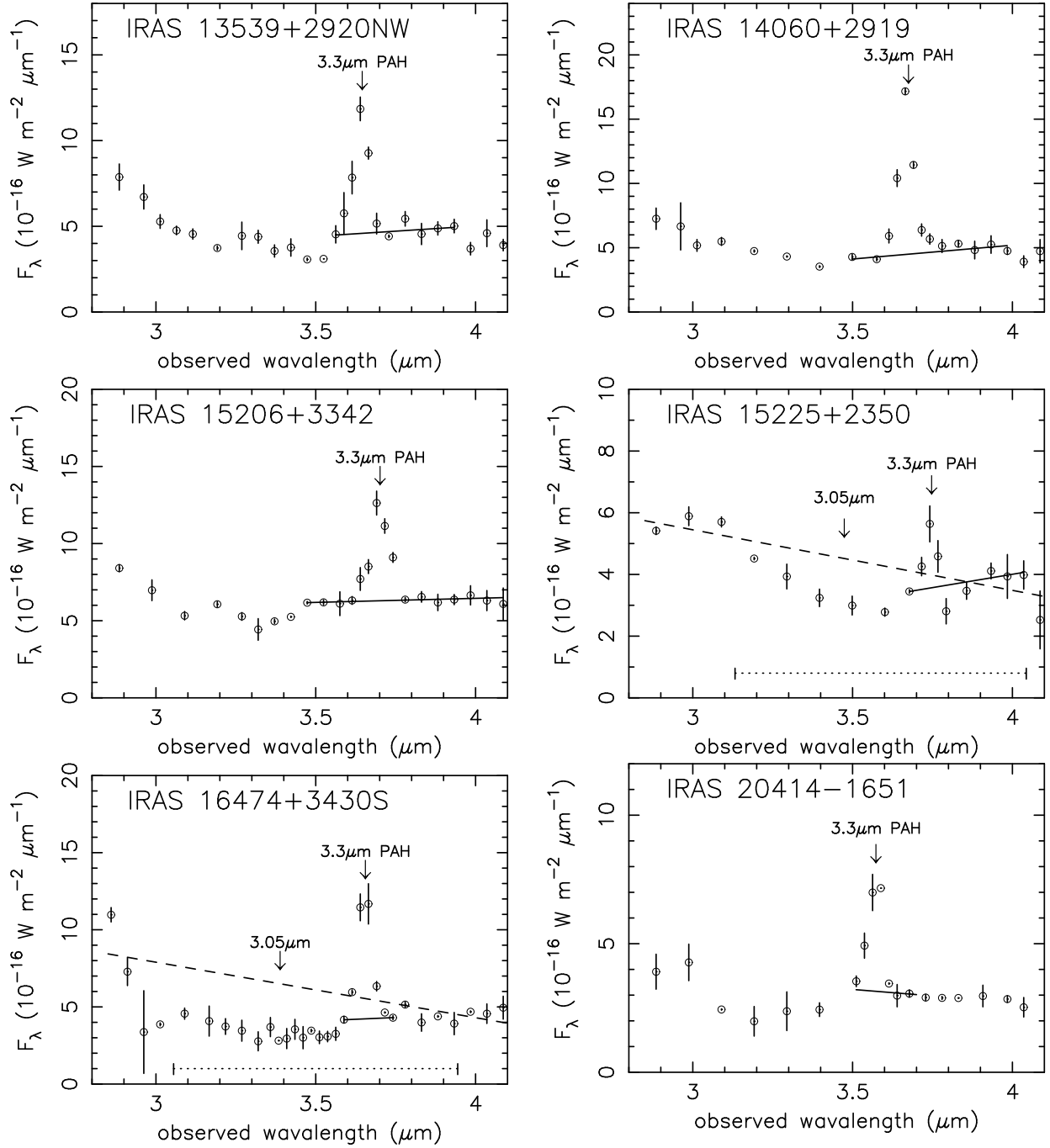


Fig. 1.— Infrared  $L$ -band ( $\lambda_{\text{obs}} = 2.8\text{--}4.1 \mu\text{m}$ ) spectra of ULIRGs’ nuclei classified optically as LINERs. The abscissa and ordinate are the observed wavelength in  $\mu\text{m}$  and  $F_{\lambda}$  in  $10^{-16} \text{ W m}^{-2} \mu\text{m}^{-1}$ , respectively. The lower arrows with “ $3.3 \mu\text{m}$  PAH” indicate the expected wavelength of the  $3.3 \mu\text{m}$  PAH emission ( $\lambda_{\text{rest}} = 3.29 \mu\text{m}$ ). The solid lines are the adopted continuum to estimate the  $3.3 \mu\text{m}$  PAH emission fluxes. The arrows with “ $3.05 \mu\text{m}$ ” or “ $3.4 \mu\text{m}$ ” indicate the expected absorption peak at  $\lambda_{\text{rest}} = 3.05 \mu\text{m}$  and  $3.4 \mu\text{m}$ , respectively. For ULIRGs with obvious signatures of these absorption features, dashed straight lines are plotted to show the adopted continuum levels used to estimate the absorption optical depths. The dotted lines indicate the wavelength range where the effects of the broad  $3.05 \mu\text{m}$  ice absorption feature can be significant ( $\lambda_{\text{rest}} = 2.75\text{--}3.55 \mu\text{m}$  adopted from the spectrum of Elias 16; Smith et al. 1989). The ice absorption feature is usually very strong at  $\lambda_{\text{rest}} = 2.9\text{--}3.2 \mu\text{m}$ , but the profiles and wavelength range of weaker absorption wings are found to vary among different Galactic objects (Smith et al. 1989).

### HII (1)



### HII (2)





### HII (3)

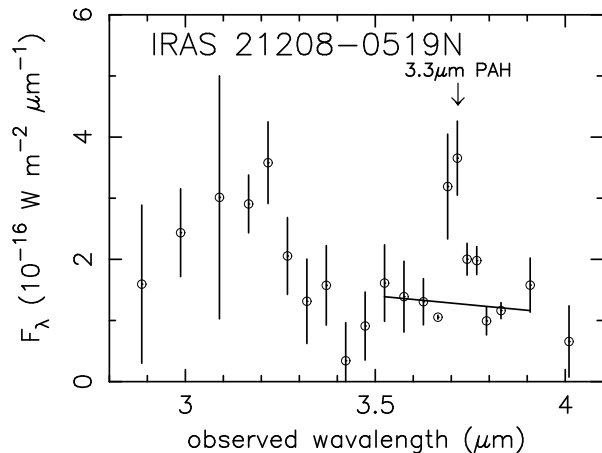


Fig. 2.— Infrared  $L$ -band ( $\lambda_{\text{obs}} = 2.8\text{--}4.1 \mu\text{m}$ ) spectra of ULIRGs classified optically as HII-regions. Units and symbols are the same as Figure 1.

### Unclassified

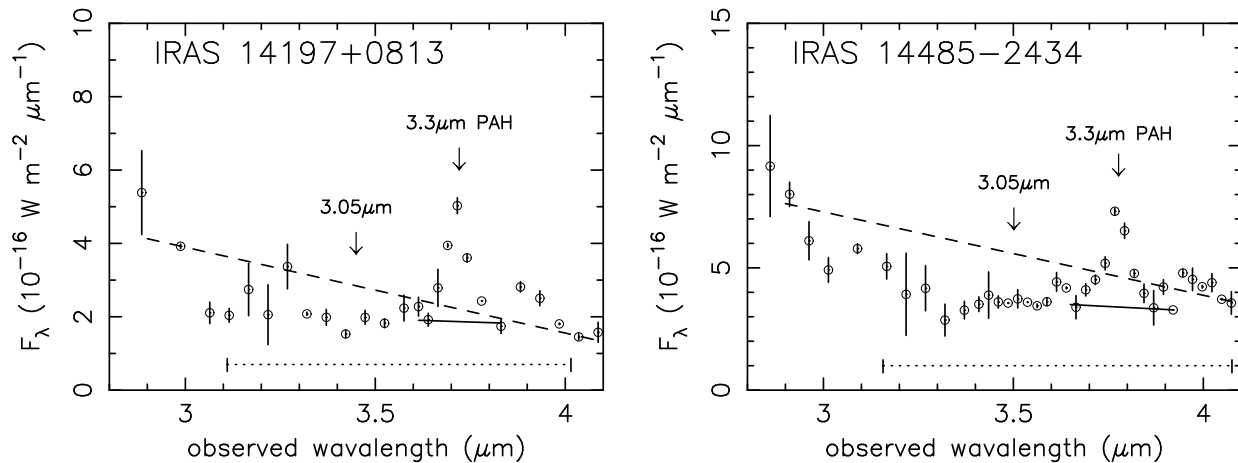
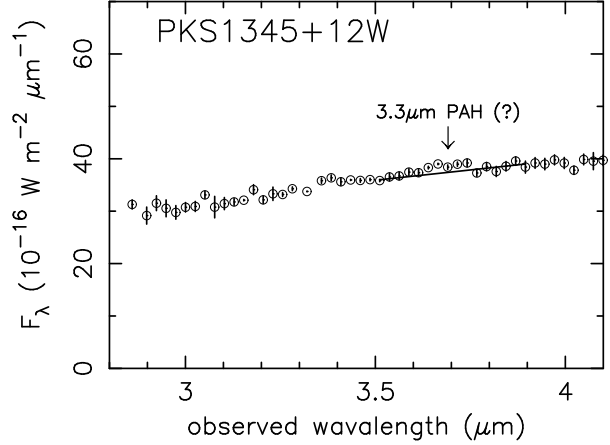
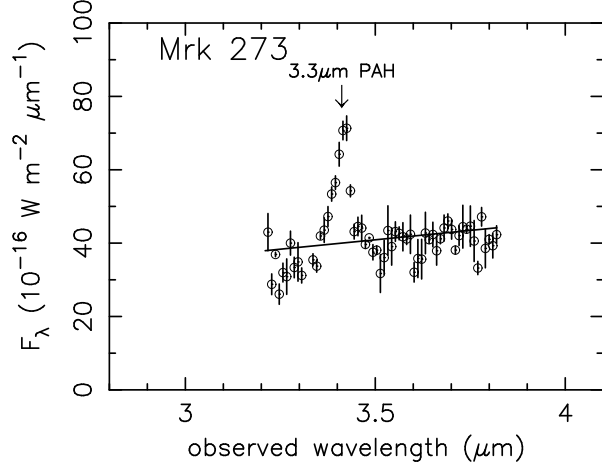
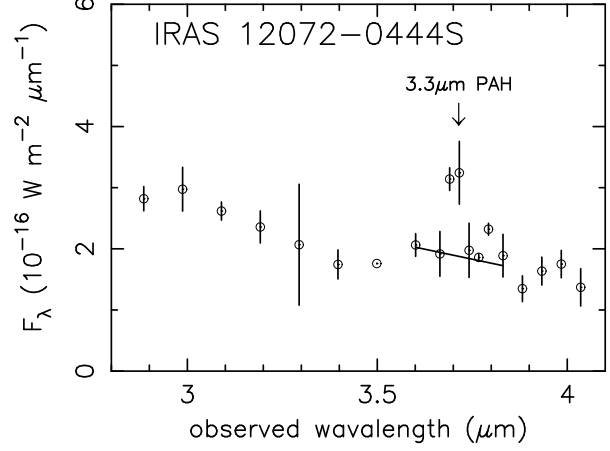
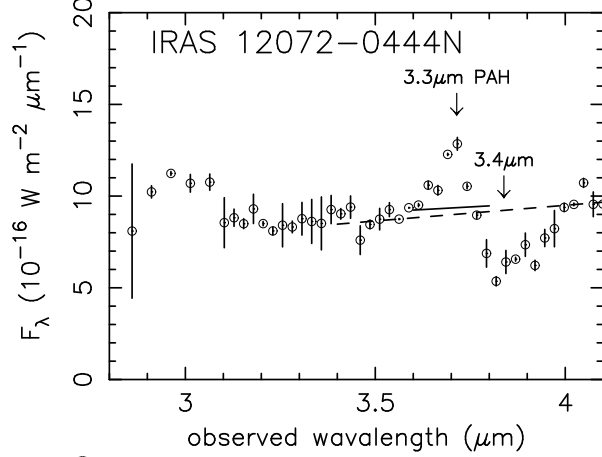
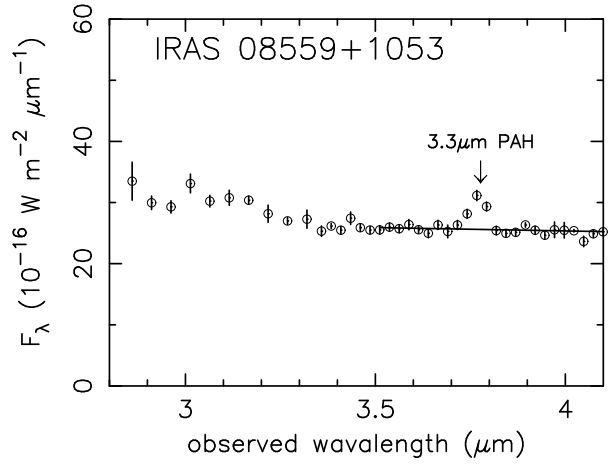
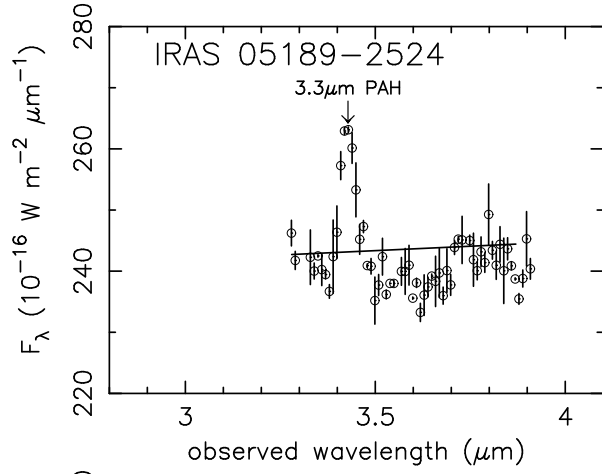


Fig. 3.— Infrared  $L$ -band ( $\lambda_{\text{obs}} = 2.8\text{--}4.1 \mu\text{m}$ ) spectra of optically unclassified ULIRGs. Units and symbols are the same as Figure 1.

## Sy2



## Sy2 (II)

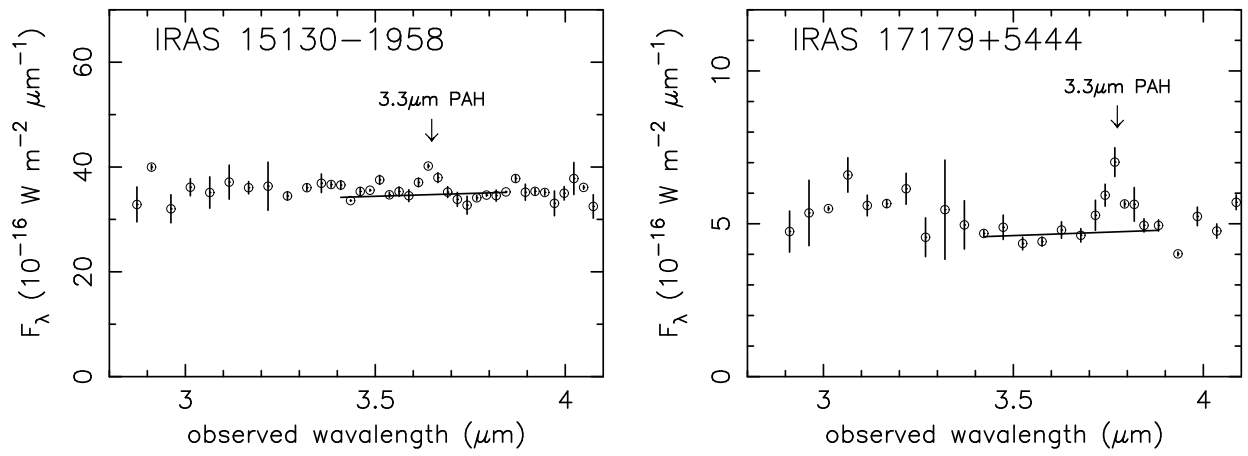
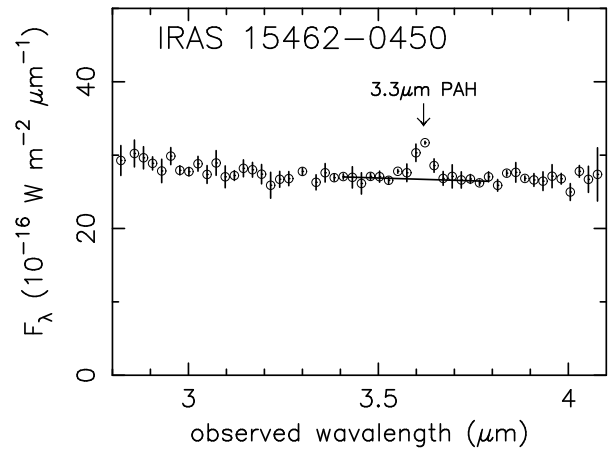
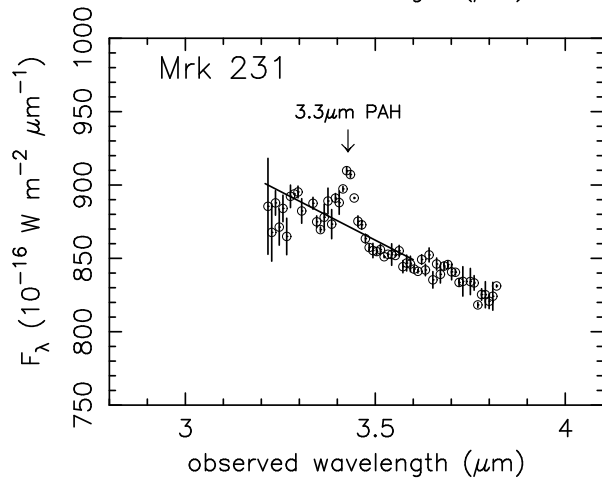
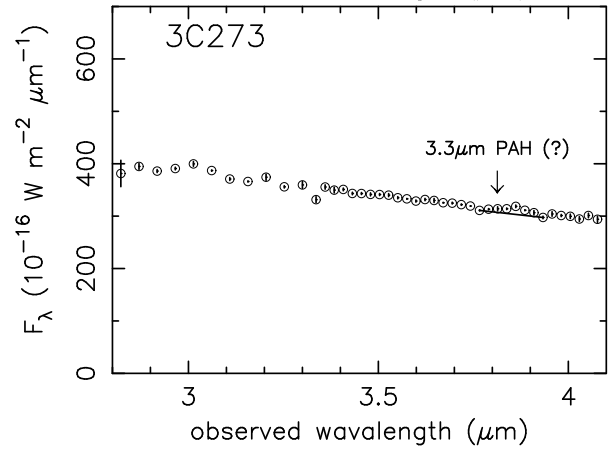
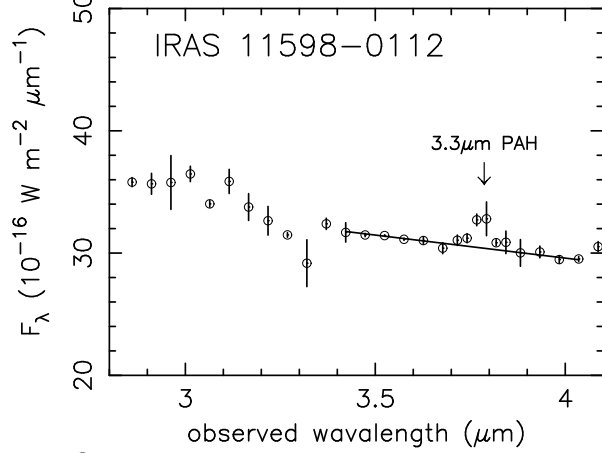
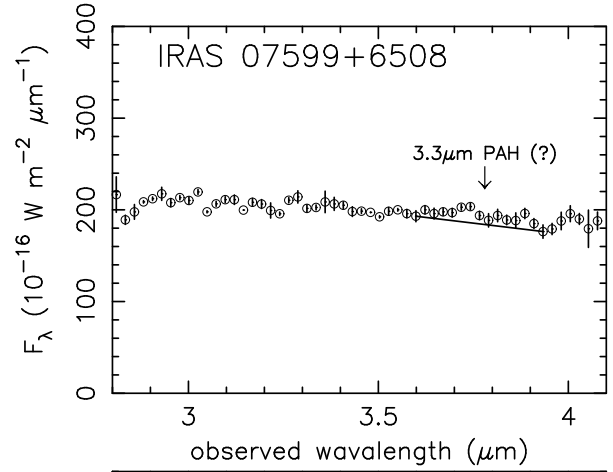
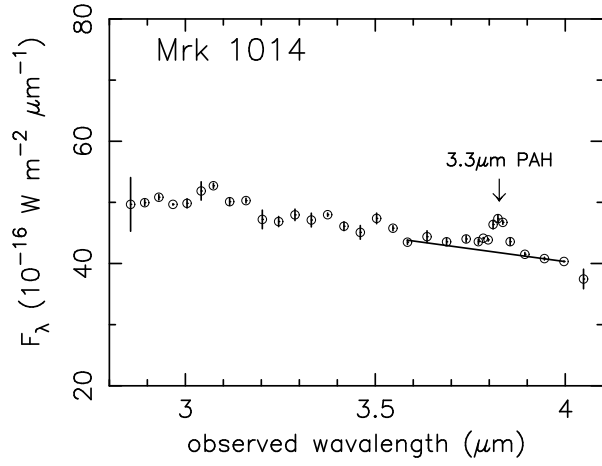


Fig. 4.— Infrared  $L$ -band ( $\lambda_{\text{obs}} = 2.8\text{--}4.1 \mu\text{m}$ ) spectra of ULIRGs classified optically as Seyfert-2s. Units and symbols are the same as Figure 1.

# Sy1



## Sy1 (II)

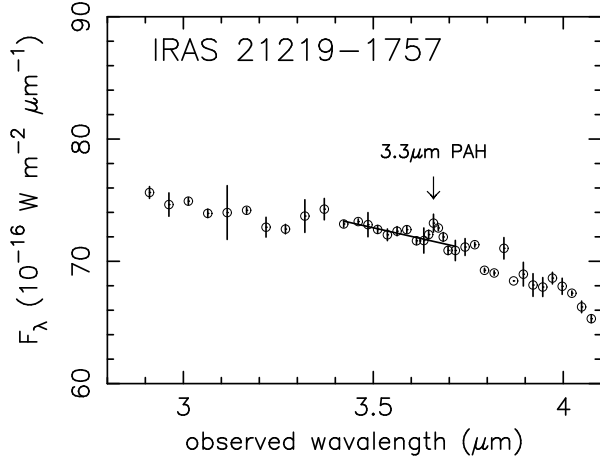


Fig. 5.— Infrared  $L$ -band ( $\lambda_{\text{obs}} = 2.8\text{--}4.1 \mu\text{m}$ ) spectra of ULIRGs classified optically as Seyfert-1s. Units and symbols are the same as Figure 1.

## K-band

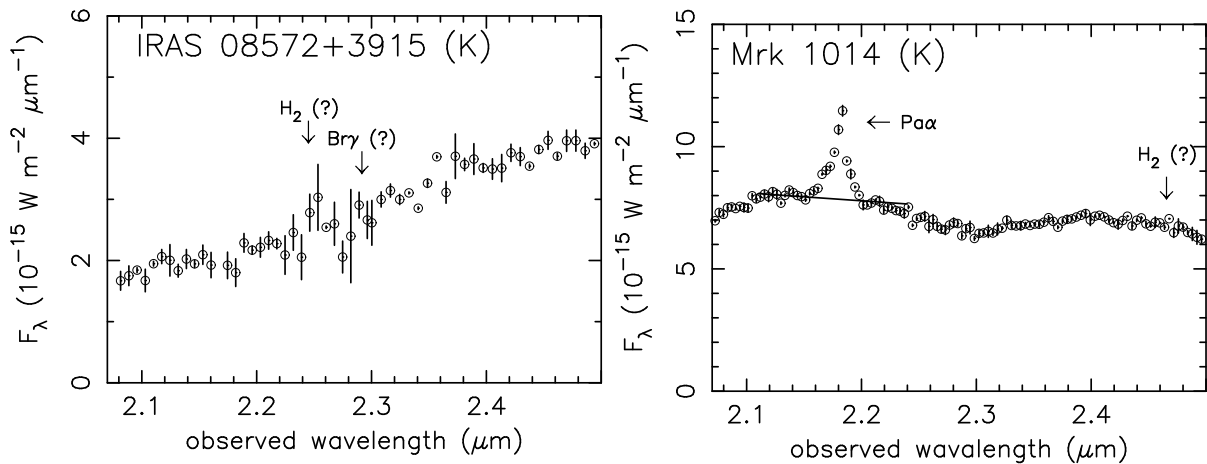


Fig. 6.— Infrared  $K$ -band ( $\lambda_{\text{obs}} = 2.07\text{--}2.5 \mu\text{m}$ ) spectra of IRAS 08572+3915 and Mrk 1014, obtained with IRTF SpeX. The abscissa is the observed wavelength in  $\mu\text{m}$ . The ordinate is  $F_{\lambda}$  in  $10^{-15} \text{ W m}^{-2} \mu\text{m}^{-1}$ . The solid line in the Mrk 1014 spectrum is the adopted continuum level to estimate the  $\text{Pa}\alpha$  emission flux.

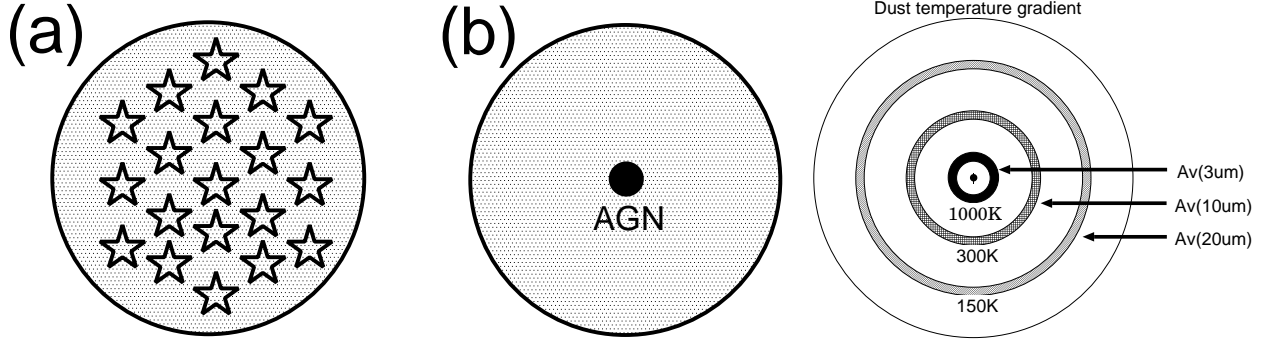


Fig. 7.— (a): Geometry of energy sources and dust in a normal starburst. The energy sources (stars) and dust are spatially well mixed. (b) (Left): Geometry of an energy source and dust in a buried AGN. The energy source is more centrally concentrated than the surrounding dust. (b) (Right): Schematic diagram of a strong dust temperature gradient around a centrally-concentrated energy source. Inner dust has higher temperature. The blackbody radiation from inner 1000K dust, close to the dust sublimation radius, has a peak at  $\lambda \sim 3 \mu\text{m}$ . That of outer 300K dust and that of even outer 150K dust have peaks at  $\lambda \sim 10 \mu\text{m}$  and  $\sim 20 \mu\text{m}$ , respectively. This is a very simplified picture, and in an actual case, dust with other temperatures can also contribute to the observed flux at each wavelength of  $3 \mu\text{m}$ ,  $10 \mu\text{m}$ , and  $20 \mu\text{m}$ . The contribution is highly dependent on the dust radial density distribution, but regardless of any dust radial density distribution, it is always true that a contribution from inner, hotter dust emission is larger at shorter wavelengths in this wavelength range. Thus, the relation  $A_V(3\mu\text{m}) > A_V(10\mu\text{m}) > A_V(20\mu\text{m})$  should hold, and dust extinction estimated using  $3 \mu\text{m}$  data is a better probe for dust column density toward the AGN itself than longer wavelengths. Dust extinction toward  $3 \mu\text{m}$  continuum emitting region,  $A_V(3\mu\text{m})$ , can be estimated from  $\tau_{3.4}$  (bare dust) and  $\tau_{3.1}$  (ice-covered dust) values. Dust extinction toward  $10 \mu\text{m}$  and  $20 \mu\text{m}$  continuum emitting regions,  $A_V(10\mu\text{m})$  and  $A_V(20\mu\text{m})$ , can be estimated from the optical depths of  $9.7 \mu\text{m}$  and  $18 \mu\text{m}$  silicate dust absorption features, respectively. These  $A_V(10\mu\text{m})$  and  $A_V(20\mu\text{m})$  data will be available for all the non-Seyfert ULIRGs studied in this paper from Spitzer IRS spectra of guaranteed time observations and Cycle-1 programs, including ours. Comparison of these values can be used to further investigate whether the energy source is more centrally concentrated than the surrounding dust (Dudley & Wynn-Williams 1997; Imanishi 2000).

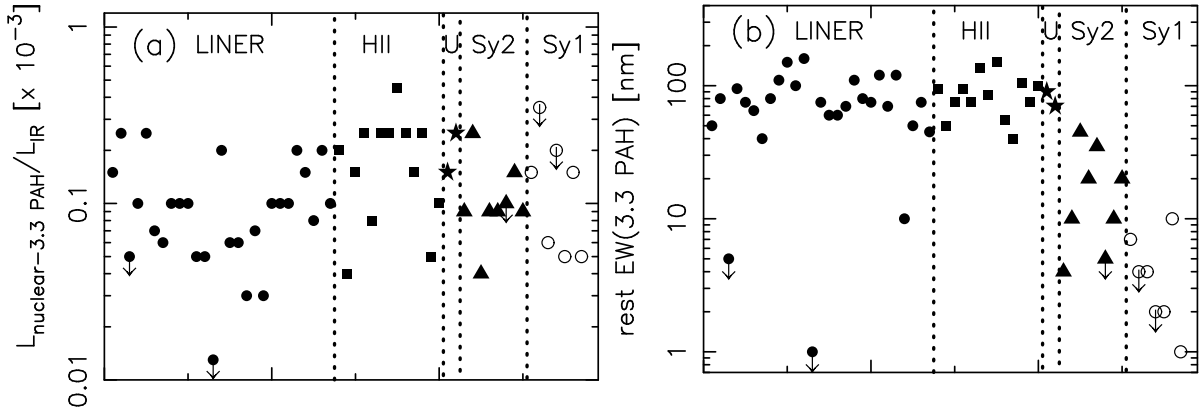


Fig. 8.— (a): Observed nuclear  $3.3 \mu\text{m}$  PAH to infrared luminosity ratio, separated by optical spectral types. ULIRGs’ nuclei classified optically as LINERs, HIIs, unclassified, Seyfert 2s, Seyfert 1s (from the left to the right) are separated by the vertical dashed lines. Filled circles: LINER. Filled squares: HII. Filled stars: optically unclassified. Filled triangles: Seyfert-2. Open circles: Seyfert-1. Objects’ order is the same as that shown in Table 3. The data point of IRAS 12127–1412 ( $\text{EW}_{3.3\text{PAH}} = 0 \text{ nm}$ ) is plotted at the lowest visible part in this Figure. (b): Rest frame equivalent widths of the  $3.3 \mu\text{m}$  PAH emission, separated by optical spectral types. Symbols are the same as (a).

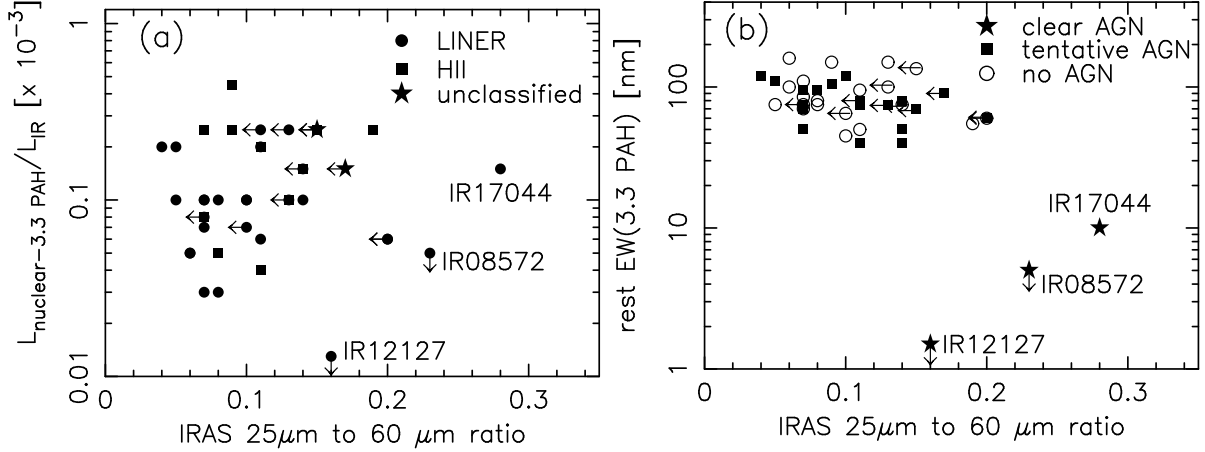


Fig. 9.— (a): Observed nuclear 3.3  $\mu\text{m}$  PAH to infrared luminosity ratio (ordinate) and *IRAS* 25  $\mu\text{m}$ -to-60  $\mu\text{m}$  flux ratio (abscissa) for non-Seyfert ULIRGs’ nuclei. Filled circles: LINER ULIRGs’ nuclei. Filled squares: HII ULIRGs’ nuclei. Filled stars: optically unclassified ULIRGs’ nuclei. For several double nuclei ULIRGs, emission from individual nuclei is resolved in our *L*-band spectra, but not in the *IRAS* data. For these sources, we assume that both nuclei have the same far-infrared colors as measured with *IRAS*. The data points of three LINER ULIRGs powered by almost pure buried AGNs, IRAS 08572+3915NW, 12127–1412NE, and 17044+6720, are indicated as “IR08572”, “IR12127”, and “IR17044”, respectively. The data point of IRAS 12127–1412 ( $\text{EW}_{3.3\text{PAH}} = 0$  nm) is plotted at the lowest visible part in this Figure. (b): Rest frame equivalent widths of the 3.3  $\mu\text{m}$  PAH emission (ordinate) and *IRAS* 25  $\mu\text{m}$ -to-60  $\mu\text{m}$  flux ratio (abscissa) for non-Seyfert ULIRGs. Filled stars: ULIRGs with clear buried AGN signatures. Filled squares: ULIRGs with tentative buried AGN signatures. Open circles: ULIRGs with no obvious buried AGN signatures in our *L*-band spectra. The data points of IRAS 08572+3915NW, 12127–1412NE, and 17044+6720 are indicated in the similar way to (a).